

Different $\alpha_2\delta$ Accessory Subunits Regulate Distinctly Different Aspects of Calcium Channel Function in the Same *Drosophila* Neurons

Abbreviated Title: Two $\alpha_2\delta$ subunits with distinct functions in the same neuron

Laurin Heinrich and Stefanie Ryglewski*

Institute of Developmental Biology and Neurobiology,
Johannes Gutenberg University Mainz
Hanns-Dieter Hüsch Weg 15, 55128 Mainz
Germany

Corresponding author: *Stefanie Ryglewski at the above address.

Email: ryglewsk@uni-mainz.de

Acknowledgments: Support from the German Research Foundation (Deutsche Forschungsgemeinschaft, DFG) to SR is gratefully acknowledged (RY117/3-1). We thank Dr. Duch (Mainz) for many helpful discussions and comments on the ms.

The authors declare no conflict of interest.

Abstract

Voltage gated calcium channels (VGCCs) regulate neuronal excitability and translate activity into calcium dependent intracellular signaling. The pore forming α_1 subunit of high voltage activated (HVA) VGCCs operates not in isolation but associates with $\alpha_2\delta$ accessory subunits. $\alpha_2\delta$ subunits can affect calcium channel biophysical properties, surfacing, localization and transport, but their *in vivo* functions are incompletely understood. In vertebrates, it is largely unknown whether different combinations of the four $\alpha_2\delta$ and the 7 α_1 subunits mediate different or partially redundant functions or whether different $\alpha_1/\alpha_2\delta$ combinations regulate different aspects of VGCC function. This study capitalizes on the relatively simpler situation in the *Drosophila* genetic model that contains only two genes for HVA calcium channels, one Ca_v1 homolog and one Ca_v2 homolog, both with well-described functions in different compartments of identified motoneurons. We find that both $\alpha_2\delta_1$ and $\alpha_2\delta_3$ (*stj*) are broadly but differently expressed in the nervous system. Both are expressed in motoneurons, but with differential subcellular localization. Functional analysis reveals that $\alpha_2\delta_3$ is required for normal Ca_v1 and Ca_v2 current amplitudes and for correct Ca_v2 channel function in all neuronal compartments, axon terminal, axon, and somatodendritic domain. By contrast, $\alpha_2\delta_1$ does not affect Ca_v1 or Ca_v2 current amplitudes or presynaptic function, but it is required for correct Ca_v2 channel allocation to the axonal versus the dendritic domain. Therefore, different $\alpha_2\delta$ subunits are required in the same neurons to precisely regulate distinctly different functions of HVA calcium channels, which is in accord with specific $\alpha_2\delta$ mutations causing different brain diseases.

Significance Statement

Calcium influx through the pore forming α_1 -subunit of voltage gated calcium channels serves essential neuronal functions, such as synaptic vesicle release, control of action potential shape and frequencies, synaptic input computations, and transcriptional control. Localization and function of α_1 -calcium channel subunits depend on interactions with $\alpha_2\delta$ accessory subunits. Here we present *in vivo* analysis of *Drosophila* motoneurons revealing that different $\alpha_2\delta$ subunits independently regulate distinctly different aspects of calcium channel function in the same neuron, such as current amplitude and dendritic versus axonal channel localization. Our findings start unraveling how different $\alpha_1/\alpha_2\delta$ combinations regulate functional calcium channel diversity in different sub-neuronal compartments, and may provide an entry point toward understanding how mutations of different $\alpha_2\delta$ genes underlie brain diseases.

Introduction

$\alpha_2\delta$ -accessory subunits affect multiple aspects of neuronal high voltage activated calcium channel (HVA VGCC) function (Brockhaus et al., 2018; Ferron et al., 2018; Tong et al., 2017; Fell et al., 2016; Hoppa et al., 2012). Consequently, mutations in $\alpha_2\delta$ genes are cause to neurological conditions such as ataxia (Calandre et al., 2016; Davies et al., 2007; Klugbauer et al., 2003), epilepsy (Faria et al., 2017; Celli et al., 2017; Dolphin, 2012; 2013), and neuropathic pain (Chen et al., 2019; Nieto-Rostro et al., 2018, Bauer et al., 2009). However, despite numerous reports on the roles of $\alpha_2\delta$ subunits in HVA channel trafficking (Kadurin et al., 2017; Hendrich et al., 2008), surfacing (D'Arco et al., 2015; Cassidy et al. 2014), and biophysical properties (Savalli et al., 2016; Davies et al., 2010, Felix et al., 1997, Hobom et al., 2000, Cantí et al., 2005), the specific *in vivo* functions that may result from different $\alpha_2\delta/\alpha_1$ combinations remain incompletely understood. In heterologous expression systems, full calcium current amplitudes require co-expression of $\alpha_2\delta$ and β with the pore forming HVA VGCC α_1 subunit (Barclay et al., 2001; Brodbeck et al., 2002; Davies et al., 2006; 2010; Cantí et al., 2005; Hoppa et al., 2012; for review see Dolphin, 2013), largely independent of which $\alpha_2\delta$ subunit is used, indicating redundant functions of $\alpha_2\delta$ subunits. By contrast, mutations of single $\alpha_2\delta$ subunit genes cause brain disease, rendering functional redundancy unlikely to occur *in vivo*. In fact, different $\alpha_2\delta$ subunits show differential spatial expression in the vertebrate brain (Scott and Kammermeier, 2017; Nieto-Rostro et al., 2014; Cole et al., 2005). A fundamental question thus is whether different combinations of $\alpha_2\delta$ and α_1 subunits mediate distinctly different functions in neurons, what these are *in vivo*, and whether a combinatorial code of different $\alpha_2\delta/\alpha_1/\beta$ combinations regulates subcellular aspects of HVA channel function *in vivo*.

The 7 vertebrate HVA VGCC genes (Catterall, 2011) comprise two families, four Ca_v1 channels ($\text{Ca}_v1.1$ - $\text{Ca}_v1.4$) and three Ca_v2 channels ($\text{Ca}_v2.1$ - $\text{Ca}_v2.3$). In combination with four genes each for β - and $\alpha_2\delta$ -subunits (reviewed in Buraei and Yang, 2010; Dolphin, 2013), this totals to > 100 possible combinations of $\alpha_1/\beta/\alpha_2\delta$ HVA VGCC complexes. All so far tested $\alpha_1/\beta/\alpha_2\delta$ combinations are functional in heterologous expression systems, but it remains unclear how many of these are used *in vivo* to regulate different neuronal functions. To address this question we employ specific advantages of the *Drosophila* genetic model, which contains only one gene each homologous to the vertebrate Ca_v1 and Ca_v2 channel families. *Dmca1D* is homologous to the entire Ca_v1 family, and *Dmca1A*, also named *cacophony*, to the Ca_v2 family (Littleton and Ganetzky, 2000). Together with one β - and four genes encoding $\alpha_2\delta$ -subunits, this results in 8 possible combinations. Moreover, the relative simplicity, experimental accessibility, and available genetic tools make *Drosophila* a suitable system to study which $\alpha_2\delta/\alpha_1$ combinations regulate which aspects of neuronal HVA channel functional diversity *in vivo*. We restricted the analysis to $\text{d}\alpha_2\delta_1$ and $\text{d}\alpha_2\delta_3$ subunits because high throughput expression data reveals high expression in the CNS (flybase.org). By contrast, $\text{d}\alpha_2\delta_2$ is reported muscle specific (Reuveny et al., 2018), and a predicted $\text{d}\alpha_2\delta_4$ lacks the double cache domain and shows little mRNA expression in the CNS.

We find differential expression of both $\alpha_2\delta$ subunits throughout the nervous system and during development. Surprisingly, both are expressed in larval and adult motoneurons, but localize to different subcellular compartments and mediate distinctly different functions. $\text{d}\alpha_2\delta_3$ is required for normal somatodendritic Ca_v1 and Ca_v2 current amplitudes, as well as for correct axonal and presynaptic Ca_v2 channel function. By contrast, $\text{d}\alpha_2\delta_1$ is not required for presynaptic function or normal HVA current amplitudes but is critical for correct Ca_v2 channel allocation to the axonal versus the dendritic domain. Thus different $\text{d}\alpha_2\delta$ subunits are required in the same neuron to cooperatively regulate distinctly different aspects of HVA channel function and localization.

Materials and Methods

Drosophila melanogaster were reared at 25°C, on a 12/12hrs light/dark cycle, in plastic vials on a cornmeal, glucose, yeast, agar diet (for 6 liters: 725.69g glucose, 343.06g cornmeal, 66g Agar and 181.38g active dry yeast; after cooling to 70°C 76.25 ml Tegosept (10% in 100% ethanol) were added. After cooling to 65°C 3.5g ascorbic acid were added). Food was covered and left for 1 day at 4°C to cool and harden.

Experiments were carried out either in 2-5 day-old adult male and female, pupal stage P8 (Bainbridge and Bownes, 1981), and third instar larval animals of varying genotypes (for full list of genotypes see tables 1 and 2).

The *Drosophila* gene CG4587 is predicted to encode an $\alpha_2\delta$ subunit (Flybase) but until now no functional data existed. CG4587 was listed as the first $d\alpha_2\delta$ subunit (Kurshan et al., 2009). We used this list to name CG4587 $d\alpha_2\delta_1$. However, we do not claim that $d\alpha_2\delta_1$ fully resembles vertebrate $\alpha_2\delta_1$.

Climbing Assay

2-4 day old single male or female virgins were put in separate plastic vials one day before testing. The climbing behavior was filmed, while a ruler was placed beside the vial as a measure of length. Gently hitting the vial on the ground will induce upwards climbing behavior due to negative geotaxis. Since flies tend to be more inactive during midday, testing was always done between 9:00am-1:00pm or 3:00-5:00pm at 25 °C. The climbing speed was analyzed manually with the Avidemux software. Length and duration of climbing attempts were measured to estimate the climbing speed. Mean climbing speed was calculated from three climbing events per fly.

Immunocytochemistry

Immunohistochemistry for $stj^{mCherry}$ and $d\alpha_2\delta_1^{GFP}$ was conducted using antibodies against fluorescent epitopes that were fused to stj and $d\alpha_2\delta_1$ and genomically expressed because antibodies against *Drosophila* $\alpha_2\delta$ subunits are not commercially available.

(1) For triple staining of α -GFP, α -mCherry and α -Brp adult flies and larvae were dissected and fixated with 4% paraformaldehyde (PFA) in 0.1 M PBS (adults: 45 min / larvae: 30 min). Preparations were washed 3 times with PBS for 20 min and then permeabilized and blocked with 10 % normal donkey serum (NDS) in PBS-TritonX (0.5 %) for 5x60 min. Primary antibodies (chicken anti-GFP, 1:400, Invitrogen, A10262, RRID:AB_2534023; mouse anti-Brp, 1:200, nc82, DSHB, RRID:AB_2314867; rat anti-mCherry, 1:5000, 16D7, cat# M11217) were diluted in 10% NDS in PBS-TritonX (0.3 %) and incubated at 4 °C overnight, shaking. Afterwards the preparations were washed with PBS 8 x 30 min and then incubated with secondary antibodies (donkey anti-chicken Cy2, 1:400, Dianova, cat# 703-505-155; donkey anti-rat Cy3, 1:400, Invitrogen, A-21209; donkey anti-mouse Cy5, 1:400, Invitrogen, A-31357) in PBS at 4 °C overnight, shaking. After washing the preparations 6 x 30 min in PBS, they were dehydrated with an ascending series of 50%, 70%, 90% and 100% ethanol for 10 min each and mounted in methylsalicylate.

(2) The staining of α -HA was done as described in (1). Instead of NDS, 5% bovine serum albumin (BSA) in PBS-TritonX (0.5 %) solution was used for blocking and permeabilization of the preparations. The primary antibodies (rat anti-HA, 1:100, Roche life science, 11867423001) were diluted in 5% BSA + PBS-TritonX (0.3 %). The secondary antibodies (donkey anti-rat Cy5, 1:400, Jackson Immuno Research, 712-605-150) were diluted in PBS.

Quantification of axonal cac^{GFP} label

For live detection of axonal cacophony^{GFP} (cac; Ca_v2^{GFP}) label, a genomically tagged and endogenously expressed cacophony carrying an N-terminal GFP-tag was used (Gratz et al., 2019).

For quantification of axonal cac^{GFP} label all preparations were treated exactly the same way. 2-3 day old flies were dissected and instantly fixated with ice-cold 100% ethanol for 10 min. After washing the preparation with PBS for 10 min it was mounted in Vectashield (Vector Laboratories, Lot# X1215) and directly scanned with a Leica TSC SP8 Laser Scanning Microscope (Leica Microsystems Inc., RRID:SSR_004098) with excitation wavelength at 488 nm (Argon laser). All samples were scanned with a 20x glycine objective, a zoom factor of 1.8 for further magnification, a z-step size of 0.3 μm and an image resolution of 1024x1024 pixels. Furthermore, laser and detector settings were always identical and the laser was always warmed up 1 h before images were taken.

Projection views of the axons from stacks of 10 sections were analyzed with Fiji ImageJ 64 V5. To calculate the intensity of the axonal cac^{GFP} label a section of the axon, shortly after leaving the ventral nerve cord, was encircled and the mean gray value was measured. Per fly, the mean axonal cac^{GFP} intensity was calculated from the axons of both sides.

Western Blotting

L3 larvae were stunned on ice for 5 min and dissected in ice-cold saline. Afterwards the CNS ($\alpha_2\delta_1$ ^{GFP}: 20; stj^{mCherry}: 30) were collected in 70 μl ice-cold 2xSDS sample buffer (25ml 4x Tris Cl/SDS pH 6.8, 20ml glycerol, 4g SDS, 0.31g DTT, 1 mg Bromophenol Blue, add to 100ml with ddH₂O), homogenized and boiled at 96 °C for 3 min. Samples were then stored at -28 °C.

Discontinuous SDS-PAGE in a large Hoeffer gel chamber with 1.5 mm thickness and 15 pockets with 100 μl volume each was done. A 5 % (bis-acrylamide) stacking gel (6.8 ml ddH₂O, 1.7 ml 30% bis-acrylamide, 1.25 ml 4x Tris/SDS pH 6.8, 100 μl 10% ammonium persulfate, 10 μl TEMED) and an 8% (bis-acrylamide) running gel (18.6 ml ddH₂O, 10.7 ml 30% bis-acrylamide, 10 ml 4xTris/SDS pH 8.8, 400 μl 10% ammonium persulfate, 16 μl TEMED) was poured and polymerized at 37 °C. Afterwards the pockets were washed with SDS-glycine-Tris electrophoresis buffer (3 g Tris base, 14.4 g glycine, 1 g SDS, add to 200ml with ddH₂O). Samples were again boiled at 96 °C and centrifuged at 10,000 g for 1 min before loading. As a marker 70 μl of Color Protein Standard Broad Range (New England BioLabs, #P7712S; 25 to 245 kD) diluted 1/7 in SDS sample buffer was loaded. The gel was run at 0.02 A until the dye front passed the stacking gel, then the current was increased to 0.03 A (PowerPac, Bio-Rad).

Proteins were blotted onto nitrocellulose in a large wet tank filled with transfer buffer (18.2g Tris base, 86.5g glycine, 900 ml methanol add ddH₂O to 6L). The blotting of the proteins was done at 4 °C overnight at 40 V (PowerPac, Bio-Rad).

After blotting, the membrane was cut in half at about 80 kDa. The two membrane pieces were washed with ddH₂O for 10 min, incubated with TBST (10 ml 1M Tris pH 7.5, 30 ml 5 M NaCl, 1 ml Tween20 add to 1000 ml with ddH₂O) 3 times for 20 min and blocked with 10% dried milk-TBST solution or BlockAce-TBST solution (BlockAce, Bio-Rad, #170223) for 2 h. After washing the membrane pieces in TBST for 3 times 20 min, they were incubated separately with primary antibody (245-80 kDa: rabbit anti-GFP, 1:1,000, Life Technologies, A11122 / rabbit anti-mCherry, 1:1,000, Abcam [EPR20579]; 80-25 kDa: mouse anti-actin, 1:10,000, dshb JLA20) diluted in 2,5 % milk-TBST or 25% BlockAce-TBST solution at 4 °C overnight. Both membrane pieces were then separately washed with TBST 3 times for 20 min before incubation with secondary antibodies (245-80 kDa: goat anti-rabbit IgG, 1:10,000, Jackson ImmunoResearch, cat# 111-035-144; 80-25 kDa: goat anti-mouse IgG,

1:4,000, Millipore, 12-349) diluted in TBST for 2 h at 25 °C. After washing the membrane pieces 3 times for 20 min with TBST and 20 min with TBS membrane was incubated in Immobilon Western chemiluminescent HRP substrate (Millipore, cat# WBKLS0500) for 5 min. Bands were detected with a Fusion SL Camera and Fusion software (Vilber Lourmat). For analysis a profile blot of the western was done with Fiji ImageJ V5 and the integrated areas of the bands of interest were measured. The relative densities were calculated by dividing the bands of interest with their respective loading control (actin).

Generation of *stj*^{mCherry} flies

Flies with endogenously mCherry-tagged *stj* were generated, as already described, with a *Minos* mediated integration cassette (MiMIC) (Venken *et al.*, 2011). A MiMIC cassette is flanked by two inverted ϕ C31 bacteriophage attP sites and contains a gene-trap cassette and the yellow⁺ marker. ϕ C31 expression was driven by the *vasa* promoter. Flies with a MiMIC construct in a coding intron of *stj* were obtained from Bloomington Drosophila Stock Center (BDSC_34109) and a for the splicing phase (phase 0) compatible plasmid containing the *mCherry* sequence was obtained from the Drosophila Genomics Resource Center (DGRC #1299_pBS-KA-attB1-2-PT-SA-SD-0-mCherry; Venken *et al.*, 2011).

Female virgins of a *vasa* integrase line (BDSC_36312) were crossed with the *stj*-MiMIC flies (BDSC_34109). F1 Stage 2 embryos were injected with the DNA solution containing the mCherry plasmid (300-400 ng/ μ l). The injection electrodes (Science Products, GB100TF-8P) were pulled with a Flaming/Brown micropipette puller (Sutter Instruments Co., Model P-97) and broken individually. Injections were conducted with a Femtojet Injector (Eppendorf, cat# 5253000017) in Voltalef 10s oil. After injection, embryos were covered with Voltalef 3S oil and kept on 25 °C. Hatched larvae were then raised on instant fly food. Every hatched fly was crossed individually with either female virgins or males of a balancer stock (*y*^{1w*}; *Cyo/Sna*^{Sco}). F1 offspring displaying the yellow phenotype were re-crossed with balancer flies to build a stock. All stocks were checked for correct integration of the *mCherry* construct via PCR.

Primer sequences were obtained from Venken *et al.*, 2011: Orientation-MiL-F: GCGTAAGCTACCTTAATCTCAAGAAGAG; Orientation-MiL-R: CGCGGCGTAATGTGATTTACTATCATAC; mCherry-Seq-F: ACGGCGAGTTCATCTACAAG; mCherry-Seq-R: TTCAGCCTCTGCTTGATCTC. Four different PCR reactions (2 μ l 10x Thermopol buffer, 0.5 μ l 10mM dNTP's, 0.5 μ l F-primer, 0.5 μ l R-primer, 0.1 μ l Taq polymerase, 1 μ l DNA, 5.4 μ l ddH₂O^{RNAse free}) had to be performed for each event. The following primer combinations were used: (1) Orientation-MiL-F / mCherry-Seq-R; (2) Orientation-MiL-F / mCherry-Seq-F; (3) Orientation-MiL-R / mCherry-Seq-R; (4) Orientation-MiL-R / mCherry-Seq-F and a touchdown PCR (Biometra®, TGradient, Labexchange) was performed: 1x (94 °C, 600 s); 8x (94 °C, 30 s; 68 °C + -1 °C, 30 s; 68 °C 90 s); 32x (94 °C, 30 s; 60 °C, 30 s; 68 °C, 90 s); 1x (68 °C, 600 s). PCR products were loaded on a 0.7% agarose gel with ethidiumbromide added directly to the gel and run at 70 V (PowerPac, Bio-Rad) for about 60 min. Correct integration was marked by positive primer reactions for the primer combinations 1 & 4.

Repairing the $\alpha_2\delta_1$ ^{RNAi} stock (Vienna Drosophila Resource Center; VDRC_108150)

As previously described (Green *et al.*, 2014), during generation of VDRC "KK" RNAi stocks in rare cases the RNAi construct integrated into a second landing site (40D) in addition to the intended 30D landing site. Integration of the construct in both sites can lead to expression of a toxic protein called Tiptop (Tio). Thus, in order to prevent unspecific effects, the used KK stocks needed to be tested via PCR. Primer sequences were used as described (Green *et al.*, 2014) (C_Genomic_F: GCCCACTGTCAGCTCTCAAC; NC_Genomic_F: GCTGGCGAACTGTCAATCAC; pKC26_R:

TGTA AACGACGGCCAGT; pKC43_R: TCGCTCGTTGCAGAATAGTCC). Four primer reactions (2 μ l 10x Thermopol buffer, 0.5 μ l 10mM dNTP's, 0.5 μ l F-primer, 0.5 μ l R-primer, 0.1 μ l Taq polymerase, 1 μ l DNA, 5.4 μ l ddH₂O^{RNAse free}) had to be done for each tested line (1. C_Genomic_F / pKC26_R; 2. C_Genomic_F / pKC43_R; 3. NC_Genomic_F / pKC26_R; 4. NC_Genomic_F / pKC43_R) and a touchdown PCR was performed: 1x (95 °C, 120 s); 5x (95 °C, 15 s; 68 °C + -1 °C, 15 s; 72 °C 50 s); 29x (95 °C, 15 s; 62 °C, 15 s; 72 °C, 50 s); 1x (72 °C, 120 s). PCR products were loaded a 0.7% agarose gel with ethidiumbromide added directly to the gel and run at 70 V (PowerPac, Bio-Rad) for about 60 min.

Integration of the construct into the 40D landing site resulted in a PCR product of approx. 450 bp (C_Genomic_F / pKC26_R), while an empty site resulted in a PCR product of approx. 1050 bp (C_Genomic_F / pKC43_R). Integration of the construct into the 30D site resulted in a PCR product of approx. 600 bp (NC_Genomic_F / pKC26_R), while an empty site resulted in a PCR product of approx. 1200 bp (C_Genomic_F / pKC43_R).

For the $\alpha_2\delta_1^{RNAi}$ line (VDRC_108150) the pKC26 vector indeed integrated into both the 30D and 40D site. The unwanted 40D insertion was removed via mitotic recombination. Female $\alpha_2\delta_1^{RNAi}$ virgins (VDRC_108150) were crossed to males in which both sites were empty (VDRC_60100). Female virgins of the F1 progeny were then crossed to a second chromosome balancer stock. Putatively recombinant offspring could be pre-selected via eye color (red eyes) and were tested for one-sided recombination via PCR as described above.

***In situ* electrophysiology and calcium imaging experiments:**

Voltage clamp and current clamp experiments (Schützler et al., 2019; Kadas et al., 2017; Ryglewski et al., 2012; Ryglewski et al., 2014) and calcium imaging experiments were carried out as published (Ryglewski et al., 2017).

An upright Zeiss Axio Examiner A1 epi-fluorescence microscope with a 40x water dipping lens (Zeiss, Germany) with a fixed stage (Narishige) was used. Recordings were done at room temperature (24°C). Electrophysiological experiments were conducted from crawling MN somata in third instar larvae, and wing depressor MN somata (DLM, specifically MN5) from pupae stage P8 (~47-50 hrs after puparium formation, approx. halfway through pupal development (P50%)) and 2-5 day-old adult *Drosophila melanogaster* of each sex. Selection criterion for P8 was orange eyes as visible through the pupal case (Bainbridge and Bownes, 1981). All electrophysiological recordings were carried out in patch clamp whole cell configuration with an Axopatch 200B patch clamp amplifier (Molecular Devices), either in voltage clamp or current clamp mode. Data were digitized at a sampling rate of 50 kHz using a Digidata 1440 analog/digital converter (Molecular Devices) and low pass filtered with a 5 kHz Bessel filter. Data were acquired with pClamp 10.7 software (Molecular Devices).

The ganglionic sheath of the ventral nerve cord was focally digested and debris was carefully loosened and removed from the MN membrane with 1% *Streptomyces griseus* protease type XIV in saline using a broken patch pipette (Ryglewski et al., 2012b), and then rinsed thoroughly. Recording patch pipettes were pulled with a PC-10 vertical electrode puller (Narishige) from 1.5 mm outer and 1 mm inner diameter patch clamp glass capillaries without filament (WPI, #PG52151-4). Pipette resistance with Ca²⁺ current recording solutions was ~3.5 M Ω for pupal and adult MN5, ~4 M Ω for larval MNs, in action potential recording solutions ~6 M Ω for pupal and adult MN5, and ~6.5 M Ω for larval MNs. For solutions see below. Preparations were perfused with fresh saline (~0.5 ml/min) throughout the course of the entire experiment.

Recording solutions:

Intracellular Ca^{2+} current recording solution (in mM): 140 CsCl, 0.5 CaCl₂, 2 Mg-ATP, 11 EGTA, 20 TEA-Br, 0.5 4-AP, 10 HEPES; pH was adjusted to 7.24 with 1 N CsOH, osmolality was 327 mOsM/kg.

Extracellular Ca^{2+} current recording solution (in mM): 93 NaCl, 5 KCl, 4 MgCl₂, 1.8 CaCl₂, 1.8 BaCl₂, 30 TEA-Cl, 2 4-AP, 5 HEPES, ~35 sucrose. pH was adjusted to 7.24 with 1N NaOH, osmolality was adjusted to 320 mOsM/kg with sucrose if necessary. TTX was added directly to the bath (the perfusion was halted for 5 min) at 10^{-7}M (adults and pupae) or $4 \times 10^{-7}\text{M}$ (larvae) to block fast Na^{+} current. K^{+} channels were blocked with TEA and 4-AP.

Intracellular action potential recording solution (in mM): 140 K-gluconate, 2 Mg-ATP, 2 MgCl₂, 11 EGTA, 10 HEPES. pH was adjusted to 7.24 with 1 N KOH, osmolality was adjusted to 300 mOsM/kg with glucose if necessary.

Extracellular action potential recording solution (normal saline; in mM): 128 NaCl, 2 KCl, 4 MgCl₂, 1.8 CaCl₂, 5 HEPES, ~35 sucrose, pH was adjusted to 7.24 with 1 N NaOH, osmolality was adjusted to 290 mOsM/kg with sucrose if necessary.

Intracellular Ca^{2+} imaging solution (in mM): 140 K-gluconate, 2 Mg-ATP, 2 MgCl₂, 10 phosphocreatine di tris, 0.3 Na₂GTP, 10 HEPES. EGTA was omitted because of the presence of GCaMP6s. pH was adjusted to 7.24 with 1 N KOH, osmolality was 313 mOsM/kg.

Extracellular action potential recording solution (normal saline; in mM): 115.8 NaCl, 2 KCl, 4 MgCl₂, 5 CaCl₂, 5 HEPES, ~35 sucrose, pH was adjusted to 7.24 with 1 N NaOH, osmolality was adjusted to 305 mOsM/kg with sucrose if necessary.

Voltage clamp and current clamp experiments (incl. Ca^{2+} imaging experiments):

For voltage and current clamp recordings, offset was nulled manually while approaching the cell, applying gentle positive pressure to the patch pipette to avoid dilution of the tip with extracellular solution. After gigaseal formation, mode was changed to patch configuration (or on-cell), and the cell was clamped to -30 mV (for Ca^{2+} current recordings) or -70 mV (for AP recordings), respectively. Fast capacitance artifacts of the recording electrode were zeroed using the C-slow and C-fast dials of the amplifier, lag was 2 μs . Break-in was achieved by short and quick, gentle suction. Configuration was changed to whole cell, and cell capacitance as well as series resistance were compensated for using the whole cell cap and serial resistance dials of the amplifier. Only recordings with series resistances below 10 M Ω were continued. Usually, series resistance was ~8 M Ω . Prediction was set to ~98%, and compensation was between 40 and 50%. In Ca^{2+} current experiments, the cell was manually clamped to -70 mV in 20 mV increments, once all parameters were compensated. This was necessary because the Goldman potential with the given solutions was around 0 mV and therefore far away from the intended holding potential of -70 mV. Clamping the cell to -70 mV immediately often results in rupture.

Ca^{2+} current recordings: Ca^{2+} currents were recorded in voltage clamp mode. Currents were evoked by 200 ms voltage steps from -90 mV to +20 mV (adult and pupal MNs) or 0 mV (larval MNs) from a holding potential of -90 mV in 10 mV increments. Linear leak was calculated from the first three voltage steps and subtracted offline. Adult Ca^{2+} current consists of low (LVA) and high voltage activated (HVA) currents. The fast LVA was isolated by addition of the off-artifact to the on-artifact. LVA can only be observed in isolation between -70 and -40 mV. HVA activates around -30 mV and is also carried by cacophony which makes selective block of one component impossible (Ryglewski et al., 2012).

AP recordings: After break-in, parameters were adjusted as for Ca^{2+} current recordings (s.a.) to get an idea how healthy the cell is. Then we switched to current clamp mode. Only cells with a membrane potential ≤ -55 mV were used. Pupal (P8) action potentials (Ryglewski et al., 2014) were elicited by depolarizing ramp or square current injection. For Ca^{2+} imaging experiments, a 400 ms 1 nA max. amplitude ramp current injection was performed which reliably elicited a train of action potentials.

Ca^{2+} imaging: APs were elicited as described above, and the resulting changes in GCaMP6s (Chen et al., 2013) fluorescence were recorded and analyzed. An Orca Flash 4.0 LT CMOS camera (C11440-42U; Hamamatsu Photonics K.K.) with HOKAWO 3.10 software was used for image acquisition. Exposure time was 75 ms. Image series were streamed. Raw data were exported to MS Excel, and $\Delta F/F$ was calculated by $[F(\text{firing})-F(\text{rest})]/F(\text{rest})$ (Ryglewski et al., 2017). Regions of interest (ROI) were chosen in dendrites and axon.

Intracellular muscle recordings from L3 larvae

EPSPs were recorded in HL3.1 saline with 0.5 mM Ca^{2+} (62.5 mM NaCl, 10 mM MgCl_2 , 5 mM KCl, 0.5 mM CaCl_2 , 10 mM NaHCO_3 , 5 mM Trehalose, 5 mM HEPES, 35 mM Sucrose; pH 7.24-7.25, osmolality 300-310 mOsm/kg; Feng et al., 2004). Electrodes were pulled from borosilicate glass capillaries (WPI, 1B100F-4) with a Flaming/Brown micropipette puller (Sutter Instruments Co., Model P-97). L3 larvae were dissected and the CNS was removed at the end of the dissection procedure by cutting the nerves as close to the CNS as possible. A sharp electrode (tip resistance 30 M Ω) filled with 3 M KCl was placed close to muscle M10 of a thoracic segment. As reference, a chlorinated silver wire was placed inside the bath solution. Offset and capacitance of the electrode were adjusted manually before the electrode was inserted into the muscle. Signals were amplified with an Axoclamp 2B intracellular amplifier in Bridge mode, digitized with a Digidata 1440 and recorded with pClamp 10.7 software (all Molecular Devices). Only data from muscles with a membrane potential of ≤ -50 mV were used for analysis. To evoke PSPs the respective nerve was sucked into and stimulated by a suction electrode (Sutter, BF100-50-10; broken individually). As reference, a thin silver wire wrapped around the suction electrode was used. Electrical stimuli with a duration of 0.5 ms and the minimal voltage needed (+1 V) for action potential generation were applied via an Isolated Pulse Stimulator (Model 2100, A-M Systems) and amplified by a Differential AC Amplifier (Model 1700, A-M Systems). A stimulus train of 0.5 Hz was applied for 20 s. EPSP amplitudes were analyzed with Clampfit 10.7. Per animal, the mean amplitude of 10 EPSPs was calculated.

Intracellular Dye Fill: Adult MN5 was filled as described previously (Ryglewski et al., 2017). Adult flies were dissected, and the ganglionic sheath was enzymatically digested. Then the very tip of a sharp glass microelectrode (borosilicate, outer diameter 1 mm, inner diameter 0.5 mm, with filament, Sutter BF100-50-10) pulled with a Sutter P97 Flaming Brown horizontal electrode puller was filled with a 50/50 mixture of TRITC-Dextran 3000 and Neurobiotin (both Thermo Fisher) in 2 M KAcetate. Then the shaft was filled with 2 M KAcetate leaving an air bubble between the dye-loaded tip and the KAcetate to avoid dye dilution. The electrode was connected to an intracellular amplifier (Axoclamp 2B, Molecular Devices) in Bridge mode; tip resistance was ~ 60 M Ω . After impalement of the MN soma with the sharp electrode, the dye was injected iontophoretically into the cell by application of up to 1 nA positive current. Filling quality was judged visually. After completion, the electrode was removed, and the preparation was fixed with 4% paraformaldehyde in phosphate buffered saline (PBS) for 50 minutes at room temperature. After fixation the preparation was washed at least 6x20 min with PBS, then 6x20 min with 0.5% PBS-TritonX 100, both shaking. This was followed by incubation in Streptavidin coupled to Cy3 at a concentration of 1:750 at 4°C overnight, shaking. The preparation was then rinsed a few times with PBS, and then washed at least 6x30 min with PBS. Then

the preparation was subjected to an ascending ethanol series (50, 70, 90, 100% ethanol), 10 min each, and then mounted in methylsalicylate on metal slides with a 8 mm whole with a glass cover slip glued to one side with super glue. Preparations were covered with a glass cover slip, which was sealed with nail polish. Reconstruction-ready images are generated using a Leica TSC SP8 confocal laser scanning microscope with a 40x, 1.25 NA oil lens with a 561 nm DPSS laser. Detection range was between 570 and 600 nm. Z-step size was 0.3 nm, zoom 3.5. Voxel dimensions were 86 x 86 x 290 nm (x, y, z). Dendritic structure was reconstructed from confocal image stacks after export to Amira software (AMIRA 4.1.1, FEI, Hillsboro, Oregon, US) with custom plug-ins (Schmitt et al., 2004; Evers et al., 2005).

Table S1. Fly stocks used in this study

Genotype	use	identifier
y[1] w[67c23]; Mi{PT-GFSTF.0}CG4587[Mi01722-GFSTF.0]	$\alpha_2\delta_1$ protein trap, endogenously expressing GFP fused to α_2 fragment of $\alpha_2\delta_1$, resulting in $\alpha_2\delta_1^{GFP}$ (Nagarkar-Jaiswal et al., 2015)	RRID:BDSC_59288
y[1] w[*]; Mi{PT-GFSTF.0}stj[Mi00783-mCherry.0]/CyO Tb	stj protein trap, endogenously expressing mCherry fused to α_2 fragment of stj, resulting in $stj^{mCherry}$	this study
w[1118]; P{KK106795}VIE-260B; P{y[+t7.7]v[+t1.8]=TRIP.JF01825}attP2	UAS- $\alpha_2\delta_1^{RNAiKK}$ with UAS-stj ^{RNAi} in the VALIUM10 vector (Perkins et al., 2015)	RRID:FlyBase_FBst0479962; RRID:BDSC_25807
y* w*; P{GawB}stjNP1574 / CyO, P{UAS-lacZ.UW14}UW14	stj-GAL4 (Ly et al., 2008)	RRID:DGGR_104034
w[1118]; P{KK101267}VIE-260B; P{w[+mC]=UAS-Dcr-2.D}10	UAS-stj ^{RNAiKK} with UAS-dcr2 to enhance RNAi efficacy (Dietzl et al., 2007)	RRID:FlyBase_FBst0480379; RRID:BDSC_24651
w[1118]; P{KK106795}VIE-260B; P{w[+mC]=UAS-Dcr-2.D}10	UAS- $\alpha_2\delta_1^{RNAiKK}$ with UAS-dcr2 to enhance RNAi efficacy (Dietzl et al., 2007)	RRID:FlyBase_FBst0479962; RRID:BDSC_24651
w[1118]; P{w[+mW.hs]=GawB}VGlut[OK371]	vGlut-GAL4, expressed in all motoneurons incl. larval crawling MNs	RRID:BDSC_26160
w[1118]; P{y[+t7.7] w[+mC]=20XUAS-IVS-GCaMP6s}attP40; P{y[+t7.7] w[+mC]=GMR23H06-GAL4}attP2	UAS-GCaMP6s is a genetically encoded Ca^{2+} indicator. 23H06-GAL4 from HHMI Janelia Farm GAL4 driver lines; associated gene CG8084 <i>anachronism</i> , for expression pattern see http://flweb.janelia.org/cgi-bin/flew.cgi (R23H06). 23H06-Gal4 expresses in pupal and adult DLM MNs and only very few others	RRID:BDSC_42746; 23H06-GAL4 discontinued at BDSC (available from our lab)
P{w[+mW.hs]=GawB}elav[C155]	pan-neural GAL4-driver, used for pan-neural expression of UAS-RNAi transgenes for Western Blot analysis and climbing assay	RRID:BDSC_458
w[1118]; P{w[+mC]=UAS-Dcr-2.D}2; P{y[+t7.7] w[+mC]=GMR23H06-GAL4}attP2 P{w[+mC]=UAS-myr-mRFP}2/TM6B, Tb[1]	UAS-dcr2 to enhance RNAi efficacy (Dietzl et al., 2007) along with 23H06-GAL4 with UAS-myr-mRFP on the same chromosome (Chr. 3) for easier identification of DLM MNs. for expression. Used for expression of double RNAi of stj and $\alpha_2\delta_1$	RRID:BDSC_24650; 23H06-GAL4 discontinued at BDSC (available from our lab)
w[1118]; P{y[+t7.7] w[+mC]=GMR23H06-	23H06-GAL4 along with UAS-myr-	23H06-GAL4 discontinued at BDSC

GAL4}attP2, P{w[+mC]=UAS-myr-mRFP}2/TM6B, Tb[1]	mRFP on the same chromosome (Chr. 3) for easier identification of DLM MNs.	(available from our lab); RRID:BDSC_7119
P{w[+mW.hs]=GawB}elav[C155], cac ^{sfGFP-N}	GFP tagged cacophony along with elav ^{C155} -GAL4 on the same chromosome. cacophony VGCCs are endogenously tagged with super folder (sf) GFP. GFP tag was inserted directly after the second translational start via CRISPR/cas9-based methods (Gratz et al., 2019).	RRID:BDSC_458; identifier for cac ^{sfGFP-N} not yet assigned (Gratz et al. 2019)
w[*]; P{w[+mC]=eve-GAL4.RN2}P, P{w[+mC]=UAS-mCD8::GFP.L}LL5/CyO; P{w[+mC]=Act(FRT.stop)GAL4}, P{w[+mC]=UAS-FLP.D}JD2	inducible FLP out in larval MN1s and MN1b crawling MNs to induce mosaic expression of UAS.-transgenes after second instar (eve-GAL4 is turned off before third instar)	RRID:BDSC_7475; RRID:BDSC_4540; fly strain courtesy of Dr. S. Sanyal, Calico labs, San Francisco
w[*];P{w[+mC]=UAS-mCD8::GFP.L}LL5; P{w[+mW.hs]=GawB}D42	GAL4-expression in motoneurons (incl. DLM MNs) under the control of the toll6 receptor	RRID:BDSC_8816
P{w[+mC]=UAS-FLAG-stj-HA}2/CyO; In(3L)D, D[1]/TM3, Sb[1]	HA-tagged transgene of stj	RRID:BDSC_39717
y[1] M{vas-int.B}ZH-2A w[*]; sna[ScO]/CyO, P{ry[+t7.2]=sevRas1.V12}FK1	φC31 integrase expression under the control of <i>vasa</i> , which is active in the germ line	RRID:BDSC_36312
y[1] w[*]; Mi{y[+mDint2]=MIC}stj[Mi00783]/SM6a	fly strain carrying a MiMIC within a stj intron	RRID:BDSC_34109
y[1] w[*];CyO/sna[ScO]	balancer strain	lab stock

Table S2. Genotypes used for experiments

Genotype	experiment	figure
$\gamma[1] w[67c23]; Mi\{PT-GFSTF.0\}CG4587[MI01722-GFSTF.0] / Mi\{PT-GFSTF.0\}stj[MI00783-mCherry.0]$	$\alpha_2\delta_1^{GFP}$ and $stj^{mCherry}$, co-expressed. Used for localization study by immunohistochemistry of larval and adult nervous system	Figs. 1A-Bii; D-Eii
$\gamma[1] w[67c23]; Mi\{PT-GFSTF.0\}CG4587[MI01722-GFSTF.0]$	$\alpha_2\delta_1^{GFP}$, used for localization study by immunohistochemistry	Figs. 1F, Fi
$\gamma^* w^*; P\{GawB\}stjNP1574 / P\{w[+mC]=UAS-FLAG-stj-HA\}2$	HA-tagged stj UAS-transgene expressed under the control of the stj endogenous promoter (stj -GAL4).	Figs. 1C, G
pan-neural $\alpha_2\delta_1^{GFP RNAi}$ for RNAi efficacy with Western Blot: $P\{w[+mW.hs]=GawB\}elav[C155]; Mi\{PT-GFSTF.0\}CG4587[MI01722-GFSTF.0] / P\{KK106795\}VIE-260B; P\{w[+mC]=UAS-Dcr-2.D\}10 / +$	$\alpha_2\delta_1^{RNAi}$ under the control of the pan-neural driver $elav^{C155}$ -GAL4 along with UAS-Dcr-2 to enhance RNAi efficacy in $\alpha_2\delta_1^{GFP RNAi}$ background used in Western Blot analysis of RNAi efficacy.	Figs. 2A, 2Ai
control for $\alpha_2\delta_1^{GFP RNAi}$ for RNAi efficacy with Western Blot: $P\{w[+mW.hs]=GawB\}elav[C155]; Mi\{PT-GFSTF.0\}CG4587[MI01722-GFSTF.0] / +; P\{w[+mC]=UAS-Dcr-2.D\}10 / +$	Pan-neural expression of UAS-Dcr-2 under the control of $elav^{C155}$ -GAL4 in animals with endogenous expression of $\alpha_2\delta_1^{GFP}$ as control for RNAi efficacy via Western Blot	Figs. 2A, 2Ai
pan-neural $stj^{mCherry RNAi}$ for RNAi efficacy with Western Blot: $P\{w[+mW.hs]=GawB\}elav[C155]; Mi\{PT-GFSTF.0\}stj[MI00783-mCherry.0] / P\{KK101267\}VIE-260B; P\{w[+mC]=UAS-Dcr-2.D\}10 / +$	stj^{RNAi} under the control of the pan-neural driver $elav^{C155}$ -GAL4 along with UAS-Dcr-2 to enhance RNAi efficacy in $stj^{mCherry}$ background, used in Western Blot analysis of RNAi efficacy	Figs. 2A, 2Ai
control for $stj^{GFP RNAi}$ for RNAi efficacy with Western Blot: $P\{w[+mW.hs]=GawB\}elav[C155]; Mi\{PT-GFSTF.0\}stj[MI00783-mCherry.0] / +; P\{w[+mC]=UAS-Dcr-2.D\}10 / +$	Pan-neural expression of UAS-Dcr-2 under the control of $elav^{C155}$ -GAL4 in animals with endogenous expression of $stj^{mCherry}$ as control for RNAi efficacy via Western Blot	Figs. 2A, Ai
For synaptic transmission experiments with stj^{RNAi} in larval MNs: $w[1118]; P\{w[+mW.hs]=GawB\}VGlut[OK371] / P\{KK101267\}VIE-260B; P\{w[+mC]=UAS-Dcr-2.D\}10 / +$	stj^{RNAi} under the control of vGlut-GAL4 (expression in MNs, including larval crawling MNs), used for larval muscle recordings (EPSPs)	Figs. 2A, Ai
pan-neural $\alpha_2\delta_1^{RNAi}$ in climbing assay: $P\{w[+mW.hs]=GawB\}elav[C155]; P\{KK106795\}VIE-260B / P\{w[+mC]=UAS-Dcr-2.D\}2$	pan-neural $\alpha_2\delta_1^{RNAi}$ under the control of $elav^{C155}$ -GAL4 with co-expression of Dcr-2 to enhance RNAi efficacy for testing of $\alpha_2\delta_1$ neuronal function in climbing assay.	Fig. 2B
control for climbing assay: $P\{w[+mW.hs]=GawB\}elav[C155]; P\{w[+mC]=UAS-Dcr-2.D\}2 / +$	control for climbing assay	Fig. 2B
test of compensation of $\alpha_2\delta_1^{GFP}$ in pan-neural stj^{RNAi} : $P\{w[+mW.hs]=GawB\}elav[C155]; Mi\{PT-GFSTF.0\}CG4587[MI01722-GFSTF.0] / P\{KK101267\}VIE-260B; P\{w[+mC]=UAS-Dcr-2.D\}10 / +$	stj^{RNAi} in $\alpha_2\delta_1^{GFP}$ background to test whether $\alpha_2\delta_1$ may compensate for the absence stj	Fig. 2C
test of compensation of $stj^{mCherry}$ in pan-neural $\alpha_2\delta_1^{RNAi}$: $P\{w[+mW.hs]=GawB\}elav[C155]; Mi\{PT-GFSTF.0\}stj[MI00783-mCherry.0] / P\{KK106795\}VIE-260B; P\{w[+mC]=UAS-Dcr-2.D\}10 / +$	$\alpha_2\delta_1^{RNAi}$ in $stj^{mCherry}$ background to test whether stj may compensate for the absence $\alpha_2\delta_1$	Fig. 2D
For synaptic transmission experiments with $\alpha_2\delta_1^{RNAi}$ in larval MNs: $w[1118]; P\{w[+mW.hs]=GawB\}VGlut[OK371] / P\{KK106795\}VIE-260B; P\{w[+mC]=UAS-Dcr-2.D\}10 / +$	$\alpha_2\delta_1^{RNAi}$ under the control of vGlut-GAL4 (expression in MNs, including larval crawling MNs), used for larval muscle recordings (EPSPs)	Figs. 3A, Ai

control for larval synaptic transmission experiments: w[1118]; P{w[+mW.hs]=GawB}VGlut[OK371]/+; P{w[+mC]=UAS-Dcr-2.D}10/+	expression of UAS-Dcr-2 in all MNs incl. larval crawling MNs MN1s and MN1b, control for <i>stj</i> ^{RNAi} and $\alpha_2\delta_1$ ^{RNAi} in larval muscle recordings (EPSPs)	Figs. 3A, Ai
<i>stj</i> ^{RNAi} in third instar larval MN1s and MN1b crawling MNs for Ca ²⁺ current recordings: w[*]; P{w[+mC]=eve-GAL4.RN2}P, P{w[+mC]=UAS-mCD8::GFP.L}LL5/ P{KK101267}VIE-260B; P{w[+mC]=Act(FRT.stop)GAL4}, P{w[+mC]=UAS-FLP.D}JD2/ P{w[+mC]=UAS-Dcr-2.D}10/+	Mosaic expression of <i>stj</i> ^{RNAi} under the control of the even skipped (<i>eve</i>) promoter (expression in larval MN1s and MN1b crawling MNs). <i>eve</i> is turned off before third instar (which was used here). This was prevented by driving UAS-FLP under the control of <i>eve</i> -GAL4 which cut the FRT flanked stop between actin and GAL4 so that UAS-transgene expression continued under the control of the very strong actin-promoter. UAS-mCD8::GFP was co-expressed along with UAS-Dcr-2 to enhance RNAi efficacy. UAS-transgene expression occurred in a mosaic fashion, reported by GFP. This stock was used for all larval Ca ²⁺ current recordings expressing <i>stj</i> ^{RNAi}	Figs. 3B-C
$\alpha_2\delta_1$ ^{RNAi} in third instar larval MN1s and MN1b crawling MNs for Ca ²⁺ current recordings: w[*]; P{w[+mC]=eve-GAL4.RN2}P, P{w[+mC]=UAS-mCD8::GFP.L}LL5/ P{KK106795}VIE-260B; P{w[+mC]=Act(FRT.stop)GAL4}, P{w[+mC]=UAS-FLP.D}JD2/ P{w[+mC]=UAS-Dcr-2.D}10/+	Mosaic expression of $\alpha_2\delta_1$ ^{RNAi} under the control of the even skipped (<i>eve</i>) promoter (expression in larval MN1s and MN1b crawling MNs). <i>eve</i> is turned off before third instar (which was used here). This was prevented by driving UAS-FLP under the control of <i>eve</i> -GAL4 which cut the FRT flanked stop between actin and GAL4 so that UAS-transgene expression continued under the control of the very strong actin-promoter. UAS-mCD8::GFP was co-expressed along with UAS-Dcr-2 to enhance RNAi efficacy. UAS-transgene expression occurred in a mosaic fashion, reported by GFP. This stock was used for all larval Ca ²⁺ current recordings expressing $\alpha_2\delta_1$ ^{RNAi}	Figs. 3B-C
control for <i>stj</i> ^{RNAi} and $\alpha_2\delta_1$ ^{RNAi} in third instar larval MN1s and MN1b crawling MNs for Ca ²⁺ current recordings: w[*]; P{w[+mC]=eve-GAL4.RN2}P, P{w[+mC]=UAS-mCD8::GFP.L}LL5/+; P{w[+mC]=Act(FRT.stop)GAL4}, P{w[+mC]=UAS-FLP.D}JD2/ P{w[+mC]=UAS-Dcr-2.D}10/+	Mosaic expression of UAS-Dcr-2 under the control of the even skipped (<i>eve</i>) promoter (expression in larval MN1s and MN1b crawling MNs). <i>eve</i> is turned off before third instar (which was used here). This was prevented by driving UAS-FLP under the control of <i>eve</i> -GAL4 which cut the FRT flanked stop between actin and GAL4 so that UAS-transgene expression continued under the control of the very strong actin-promoter. UAS-mCD8::GFP was co-expressed UAS-transgene expression occurred in a mosaic fashion, reported by GFP. This stock was used as control for all larval Ca ²⁺ current recordings expressing <i>stj</i> ^{RNAi} or $\alpha_2\delta_1$ ^{RNAi}	Figs. 3B-C
<i>stj</i> ^{RNAi} in adult and pupal DLM MNs for Ca ²⁺ current recordings: w[1118]; P{KK101267}VIE-260B/+; P{y[+t7.7] w[+mC]=GMR23H06-GAL4}attP2, P{w[+mC]=UAS-myr-mRFP}2/ P{w[+mC]=UAS-Dcr-2.D}10	<i>stj</i> ^{RNAi} under the control of 23H06-GAL4 (expression in DLM MNs) with UAS-myr-mRFP which results in puntate red MN label for better identification. We could not detect any negative impact on Ca ²⁺ currents or action potentials when UAS-myr-mRFP is expressed in DLM MNs. Co-expression of UAS-Dcr-2 for higher RNAi efficacy. Used for adult and pupal Ca ²⁺ current and pupal action potential recordings.	Figs. 3D-G (adult), Figs. 3H-I (pupae)
$\alpha_2\delta_1$ ^{RNAi} in adult and pupal DLM MNs for Ca ²⁺ current recordings: w[1118]; P{KK106795}VIE-260B/+; P{y[+t7.7] w[+mC]=GMR23H06-GAL4}attP2, P{w[+mC]=UAS-myr-mRFP}2/ P{w[+mC]=UAS-Dcr-2.D}10	$\alpha_2\delta_1$ ^{RNAi} under the control of 23H06-GAL4 (expression in DLM MNs) with UAS-myr-mRFP which results in puntate red MN label for better identification. We could not detect any negative impact on Ca ²⁺ currents or action potentials when UAS-myr-mRFP is expressed in DLM MNs. Co-expression of UAS-Dcr-2 for higher RNAi efficacy. Used for adult and pupal Ca ²⁺ current and pupal action potential recordings.	Figs. 3D-G (adult), Figs. 3H-I (pupae)
<i>stj</i> ^{RNAi} and $\alpha_2\delta_1$ ^{RNAi} (double RNAi) in pupal DLM MNs for Ca ²⁺ current recordings: w[1118]; P{KK106795}VIE-260B	<i>stj</i> ^{RNAi} and $\alpha_2\delta_1$ ^{RNAi} under the control of 23H06-GAL4 (expression in DLM MNs) with UAS-myr-mRFP which results in puntate red MN label for better	Figs. 3H-I

<p>/P{w[+mC]=UAS-Dcr-2.D}10; P{y[+t7.7] w[+mC]=GMR23H06-GAL4}attP2, P{w[+mC]=UAS-myr-mRFP}2/ P{y[+t7.7] v[+t1.8]=TriP.JF01825}attP2</p>	<p>identification. We could not detect any negative impact on Ca²⁺ currents or action potentials when UAS-myr-mRFP is expressed in DLM MNs. Co-expression of UAS-Dcr-2 for higher RNAi efficacy. Used for adult and pupal Ca²⁺ current and pupal action potential recordings.</p>	
<p>control for stj^{RNAi} and $\alpha_2\delta_1$^{RNAi} in adult and pupal DLM MNs for Ca²⁺ current recordings: w[1118]; ; P{y[+t7.7] w[+mC]=GMR23H06-GAL4}attP2, P{w[+mC]=UAS-myr-mRFP}2/ P{w[+mC]=UAS-Dcr-2.D}10</p>	<p>expression of UAS-Dcr-2 under the control of 23H06-GAL4 as control for single and double UAS-stj^{RNAi} and UAS-$\alpha_2\delta_1$^{RNAi}</p>	<p>Figs. 3D-G (adult), Figs. 3H-I (pupae)</p>
<p>$\alpha_2\delta_1$^{RNAi} and cac^{GFP} for axonal label: P{w[+mW.hs]=GawB}elav[C155], cac^{sfGFP-N}; P{KK106795}VIE-260B/+; P{w[+mC]=UAS-Dcr-2.D}10/+</p>	<p>pan-neurally expressed $\alpha_2\delta_1$^{RNAi} (under the control of elav^{C155}-GAL4) along with endogenously GFP-tagged cacophony VGCC channels for visualization in the axon</p>	<p>Figs. 4A, B</p>
<p>stj^{RNAi} and cac^{GFP} for axonal label: P{w[+mW.hs]=GawB}elav[C155], cac^{sfGFP-N}; P{KK101267}VIE-260B /+; P{w[+mC]=UAS-myr-mRFP}2/ P{w[+mC]=UAS-Dcr-2.D}10</p>	<p>pan-neurally expressed stj^{RNAi} (under the control of elav^{C155}-GAL4) along with endogenously GFP-tagged cacophony VGCC channels for visualization in the axon</p>	<p>Figs. 4A, B</p>
<p>control for for axonal cac^{GFP} label: P{w[+mW.hs]=GawB}elav[C155], cac^{sfGFP-N}; +/+; P{w[+mC]=UAS-Dcr-2.D}10/+</p>	<p>control visualization of cacophony^{GFP} VGCCs in the axon</p>	<p>Figs. 4A, B</p>
<p>stj^{RNAi} in pupal DLM MNs for pupal action potential recordings and adult intracellular DLM MN fill: w[*];P{KK101267}VIE-260B/ P{w[+mC]=UAS-mCD8::GFP.L}LL5; P{w[+mW.hs]=GawB}D42/ P{w[+mC]=UAS-Dcr-2.D}10</p>	<p>stj^{RNAi} under the control of D42-GAL4 (incl. expression in DLM MNs). Co-expression of UAS-Dcr-2 for higher RNAi efficacy. Used for pupal action potential recordings.</p>	<p>Figs. 4C, D; Fig. 6</p>
<p>$\alpha_2\delta_1$^{RNAi} pupal DLM MNs for pupal action potential recordings and adult intracellular DLM MN fill: w[*];P{KK106795}VIE-260B/ P{w[+mC]=UAS-mCD8::GFP.L}LL5; P{w[+mW.hs]=GawB}D42/ P{w[+mC]=UAS-Dcr-2.D}10</p>	<p>$\alpha_2\delta_1$^{RNAi} under the control of D42-GAL4 (incl. expression in DLM MNs). Co-expression of UAS-Dcr-2 for higher RNAi efficacy. Used for pupal action potential recordings.</p>	<p>Figs. 4C, D; Fig. 6</p>
<p>control for stj^{RNAi} and $\alpha_2\delta_1$^{RNAi} for pupal action potential recordings and adult intracellular DLM MN fill: w[*];P{w[+mC]=UAS-mCD8::GFP.L}LL5 /+; P{w[+mW.hs]=GawB}D42/ P{w[+mC]=UAS-Dcr-2.D}10</p>	<p>control, expresses UAS-Dcr-2 under the control of D42-GAL4</p>	<p>Figs. 4C, D; Fig. 6</p>
<p>pupal Ca²⁺ imaging upon induced action potential firing in stj^{RNAi}: w[1118]; P{y[+t7.7] w[+mC]=20XUAS-IVS-GCaMP6s}attP40/ P{KK101267}VIE-260B; P{y[+t7.7] w[+mC]=GMR23H06-GAL4}attP2/ P{w[+mC]=UAS-Dcr-2.D}10</p>	<p>stj^{RNAi} under the control of 23H06-GAL4 (expression in DLM MNs) with the genetically encoded green Ca²⁺ indicator UAS-GCaMP6s Co-expression of UAS-Dcr-2 for higher RNAi efficacy. Used for pupal Ca²⁺ imaging experiments.</p>	<p>Fig. 5</p>
<p>pupal Ca²⁺ imaging upon induced action potential firing in $\alpha_2\delta_1$^{RNAi}: w[1118]; P{y[+t7.7] w[+mC]=20XUAS-IVS-GCaMP6s}attP40/ P{KK101267}VIE-260B; P{y[+t7.7] w[+mC]=GMR23H06-GAL4}attP2/ P{w[+mC]=UAS-Dcr-2.D}10</p>	<p>$\alpha_2\delta_1$^{RNAi} under the control of 23H06-GAL4 (expression in DLM MNs) with the genetically encoded green Ca²⁺ indicator UAS-GCaMP6s Co-expression of UAS-Dcr-2 for higher RNAi efficacy. Used for pupal Ca²⁺ imaging experiments.</p>	<p>Fig. 5</p>
<p>control for pupal Ca²⁺ imaging upon induced action potential firing: w[1118]; P{y[+t7.7] w[+mC]=20XUAS-IVS-GCaMP6s}attP40/+; P{y[+t7.7] w[+mC]=GMR23H06-GAL4}attP2/ P{w[+mC]=UAS-Dcr-2.D}10</p>	<p>control, expresses UAS-GCaMP6s and UAS-Dcr-2 under the control of 23H06-GAL4</p>	<p>Fig. 5</p>
<p>y[1] M{vas-int.B}ZH-2A w[*]; sna[Sc0]/ Mi{y[+mDint2]=MIC}stj[MI00783]</p>	<p>stage two embryos ZH for injection of mCherry plasmid for generation of stj^{mCherry} protein trap strain</p>	

Results

stj and $\alpha_2\delta_1$ are differentially expressed through the CNS but co-localize in motoneurons

To assess the localization of $\alpha_2\delta_1$ (CG4587) and $\alpha_2\delta_3$ (straightjacket, *stj*) in the *Drosophila* ventral nerve cord (VNC), we used genomically tagged protein trap (Nagarkar-Jaiswal et al., 2015) fly strains (*stj^{mCherry}*, $\alpha_2\delta_1^{GFP}$, see methods). In both, the larval (Figs. 1A-C) and the adult VNC (Figs. 1D-G) *stj* (green) and $\alpha_2\delta_1$ (magenta) are broadly expressed, indicating functional relevance in many neurons. $\alpha_2\delta_1$ localizes to all neuropil regions of the larval (Figs. 1Ai, Bi) and the adult VNC (Fig. 1Di, Ei), which comprise axon terminals and dendrites and are counter-labeled with the synaptic marker, bruchpilot (*brp*, cyan, Aii, Bii, Dii, Eii; Wagh et al., 2006; Kittel et al., 2006). By contrast, *stj* was not detected in central neuropils (Figs. 1B, D, E). This differential localization pattern was also found during pupal life (not shown) thus indicating different functions of *stj* and $\alpha_2\delta_1$ at all stages of post-embryonic nervous system development. Localization of *stj* in the ganglionic cortex (somata) but not in neuropils was further confirmed by expression of an HA-tagged *UAS-stj-HA* transgene under the control of the *stj-GAL4* promoter (Figs. 1C, G). HA-label reveals *stj* expression in MN somata in the larval (Fig. 1C, asterisks) and in the adult VNC (Fig. 1G, arrows). However, we cannot exclude low expression levels below immunocytochemical detection levels of *stj* in neuropil regions. Importantly, despite their differential localization with respect to VNC synaptic neuropil and ganglionic cortex, both *stj* and $\alpha_2\delta_1$ also co-express in many neuronal somata, including identified larval crawling MNs (Figs. 1A-Aiv, white arrows in Aiii, Aiv, and Merge) and adult wing depressor (DLM) MNs (Figs. 1E-Fi). Due to the abundant localization of $\alpha_2\delta_1$ in the neuropil, expression in wing MN somata is difficult to see (Fig. 1Ei, arrow heads), but was confirmed by visual inspection of single optical sections and in pupal VNC with less dense neuropil (Figs. 1F, Fi, MN somata marked with arrow heads and dotted white circles).

To investigate the functional consequences of *stj* and $\alpha_2\delta_1$ malfunction, we targeted *stj* and $\alpha_2\delta_1$ RNAi to MNs. Knock down efficacy was determined by Western Blotting following pan-neural expression of either *stj* or $\alpha_2\delta_1$ RNAi (Fig. 2A). Although transgene expression levels in MNs may differ from average pan-neural expression levels, this approach yields a reasonable estimate of knock down efficacy. In controls, two bands were detected at the expected sizes of $\alpha_2\delta$ and α_2 alone (Ferron et al., 2018). Knock down was 64% on average for *elav^{C155}-GAL4>UAS-stj^{RNAi}* (Fig. 2Ai, left two bars) and 98% on average for *elav^{C155}-GAL4>UAS- $\alpha_2\delta_1$ ^{RNAi}* (Fig. 2Ai, right two bars).

Both $\alpha_2\delta_1$ and *stj* express in the same identified MNs, but for the following reasons they likely mediate different functions: First, *stj* localizes to somata (Fig. 1) and to neuromuscular terminals of MNs (Dickman et al., 2008; Ly et al., 2008; Kurshan et al., 2009), whereas $\alpha_2\delta_1$ is localized to somata and central neuropils. Second, *stj* loss of function is embryonic lethal but loss of $\alpha_2\delta_1$ is viable, although it significantly reduces the speed of locomotion (Fig. 2B). In addition, *stj^{RNAi}* targeted to DLM MNs causes inability to fly, but $\alpha_2\delta_1^{RNAi}$ in the same MNs does not abolish flight. Finally, pan neural knock down of either $\alpha_2\delta$ subunit did not result in compensatory upregulation of the other one as revealed by Western Blotting for *stj* following pan neuronal knock down of $\alpha_2\delta_1$ and *vice versa* (Figs. 2C, D). Therefore, we hypothesize that both $\alpha_2\delta$ subunits are required in MNs for different functions.

stj but not $\alpha_2\delta_1$ is required for normal MN Ca_v1 -like and Ca_v2 -like current amplitudes in vivo

To assess the functions of $\alpha_2\delta$ in motoneurons we targeted RNAi knock down selectively to larval crawling MNs and recorded neuromuscular transmission (Figs. 3A, Ai) and somatodendritic Ca^{2+} currents (Figs. 3B-C). An ~60% reduction of *stj* protein expression in MNs by targeted expression of *stj^{RNAi}* reduced larval neuromuscular transmission by ~50%, as revealed by current clamp recordings

of EPSPs from muscle 10 following extracellular stimulation of the motor nerve (Figs. 3A middle trace, 3Ai light gray box). By contrast, $d\alpha_2\delta_1^{RNAi}$ did not reduce the amplitude of neuromuscular transmission (Figs. 3A, right trace, 3Ai, dark gray box), indicating that $d\alpha_2\delta_1$ is not required for normal Ca_v2 channel function in MN axon terminals.

To further test whether different $d\alpha_2\delta$ subunits regulate HVA currents selectively in different sub-neuronal compartments, or different HVA channels, or both, we next recorded Ca_v1 and Ca_v2 somatodendritic Ca^{2+} current by somatic voltage clamp recordings of identified MNs. Larval MNs express Ca_v2 like channels in the axon terminal active zones (Gratz et al., 2019), but somatodendritic Ca^{2+} current is mediated by the Ca_v1 homolog, Dmca1D (Littleton and Ganetzky, 2000; Worrell and Levine, 2008; Kadas et al., 2017; Schützler et al., 2019). By contrast, adult and pupal DLM MNs use the Ca_v2 homolog, Dmca1A (cacophony, Littleton and Ganetzky 2000) for both, axon terminal (Kawasaki et al., 2004) and somatodendritic Ca^{2+} current (Ryglewski et al., 2012; 2014).

Following stj^{RNAi} , MN Ca^{2+} current amplitudes were decreased on average by 46% in larval crawling MNs (HVA Ca^{2+} current, Figs. 3B, Bi, C), by 59% (sustained HVA, Figs. 3D, Di, F) or 36% (transient LVA, Figs. 3E, G) in adult DLM MNs, and by 53% in pupal DLM MNs (HVA Ca^{2+} current, Figs. 3H, Hi, I), respectively. On the contrary, $d\alpha_2\delta_1^{RNAi}$ did not affect somatodendritic Ca^{2+} current amplitudes, neither larval Ca_v1 -like nor adult or pupal Ca_v2 -like current (Figs. 3B-I). Moreover, following knock down of both stj and $d\alpha_2\delta_1$ in the same pupal DLM MNs Ca^{2+} current amplitudes reflect that of stj knock down data (Figs. Hiii, I). In summary, stj^{RNAi} impairs both pre-synaptic function as well as somatodendritic Ca^{2+} currents but $d\alpha_2\delta_1^{RNAi}$ does not. Hence, stj seems important for normal Ca^{2+} current amplitudes independent of channel type and developmental stage. We next addressed the role of $d\alpha_2\delta_1$ for which no functional data exist up to date in *Drosophila*.

stj and $d\alpha_2\delta_1$ have opposite effects on functional VGCC expression in the axon

In addition to the prominent role of HVA VGCCs at the pre-synapse for action potential (AP) triggered synaptic vesicle release, and known dendritic functions, axonal functions of HVA channels have been described in both, larval *Drosophila* MNs (Kadas et al., 2017) and developing adult *Drosophila* wing MNs (Ryglewski et al., 2014). To visualize axonal Ca_v2 channels on the level of confocal microscopy, we used genomically GFP-tagged cacophony (Ca_v2 , Littleton and Ganetzky, 2000) channels, which have been reported to function and localize not significantly differently from native channels (Gratz et al., 2019). The arrangement of all 5 DLM wing MN axons into one axon bundle exiting the VNC towards the DLM wing depressor muscle allows visualization of GFP-tagged Ca_v2 channels in MN axons by confocal microscopy (Fig. 4A). Axonal Ca_v2^{GFP} channel label was visibly (Fig. 4A, middle panel) and statistically significantly decreased by targeted stj^{RNAi} knock down (Fig. 4B). By contrast, $d\alpha_2\delta_1^{RNAi}$ causes increased Ca_v2^{GFP} channel label in MN axons (Figs. 4A, bottom panel, 4B). Therefore, stj and $d\alpha_2\delta_1$ have opposite effects on axonal cacophony channel abundance in DLM MNs. To test whether this was caused by altered transport of cacophony channels, or by functional channels in the membrane we next recorded AP shape in current clamp mode. The DLM MN action potential is mainly carried by Na^+ , but it also contains a Ca^{2+} -component during specific stages of pupal life (⁴⁸). This Ca^{2+} component can be uncovered by bath application of the potent, ubiquitous, and irreversible VGCC blocker Cd^{2+} (500 μM) that reduces AP width in controls (Fig. 4C, upper panel, left two traces, arrow head). Following stj^{RNAi} AP width was smaller than in controls (Figs. 4C), and bath application of Cd^{2+} did not decrease AP width (Figs. 4C, D), indicating that the Ca^{2+} component was missing. These data are in agreement with a reduced expression of functional Ca^{2+} channels in MNs axons following stj^{RNAi} . By contrast, the Ca^{2+} component was even more pronounced and the AP was broadened following $d\alpha_2\delta_1^{RNAi}$ (Fig. 4C). AP shape was affected to an extent that the Ca^{2+} shoulder (Fig. 4C, top left trace, arrow head; ⁴⁸) amounted to a double peak that was abolished by application of Cd^{2+} (Figs.

4C, top and bottom traces, D). Therefore, $d\alpha_2\delta_1^{RNAi}$ likely increases the density of functional Ca_v2 channels in MN axons. A role of $d\alpha_2\delta$ subunits on axonal Ca^{2+} influx and thus AP shape is further supported by AP recordings in high Ca^{2+} recording saline (5 mM) which results in even broader APs in controls and following $d\alpha_2\delta_1^{RNAi}$ but not stj^{RNAi} (Fig. 4C, right traces). However, our data show that *stj* is required for normal pre-synaptic, somatodendritic, and axonal Ca_v2 channel function, whereas $d\alpha_2\delta_1$ is not required for normal pre-synaptic Ca^{2+} channel function, but knock down increases functional axonal Ca_v2 channel density.

stj and $d\alpha_2\delta_1$ are needed for dendritic localization of VGCCs, but only $d\alpha_2\delta_1$ sets axonal VGCC abundance

We next tested whether stj^{RNAi} and $d\alpha_2\delta_1^{RNAi}$ affected also the functional localization of VGCCs in dendrites and axon. Somatodendritic Ca^{2+} currents were decreased following stj^{RNAi} but not following $d\alpha_2\delta_1^{RNAi}$ (Fig. 3), and the Ca^{2+} component in pupal APs was abolished following stj^{RNAi} but increased following $d\alpha_2\delta_1^{RNAi}$ (Fig. 4). Thus, we expected smaller dendritic and axonal Ca^{2+} influx in stj^{RNAi} MNs and unaltered dendritic but increased axonal Ca^{2+} influx following $d\alpha_2\delta_1^{RNAi}$. We genetically expressed the Ca^{2+} indicator GCaMP6s (Chen et al., 2013, Ryglewski et al., 2017) in DLM MNs (23H06-GAL4>UAS-IVS-10xUAS-GCaMP6s) to assess potential channel mis-localization by functional imaging. We used pupal MNs because the developing VNC allows better visualization of dendritic processes as compared to the adult one, but overall localization of both $d\alpha_2\delta$ subunits through the VNC is similar during pupal and adult life. In these neurons, AP firing causes global Ca^{2+} influx through VGCC (Ryglewski et al., 2017) and was induced by somatic ramp current injection (Fig. 5C). The resulting Ca^{2+} signals were recorded from defined dendritic regions and from the axon (Fig. 5A). Unexpectedly, *stj* and $d\alpha_2\delta_1$ knock down both reduced dendritic Ca^{2+} signals by about 50% as compared to control (Figs. 5B, D) indicating a role of both $d\alpha_2\delta$ subunits for dendritic VGCC function. However, reduction in *stj* and $d\alpha_2\delta_1$ expression had opposing effects on axonal Ca^{2+} signals, as expected (Figs. 5B, Di). Axonal Ca^{2+} signals were significantly decreased following stj^{RNAi} but significantly increased following $d\alpha_2\delta_1^{RNAi}$. Given that following stj^{RNAi} Ca^{2+} entry is reduced in all compartments tested, this indicates a principal role for *stj* to target and/or surface VGCCs or to increase channel conductance. However, a role of *stj* in increasing channel conductance seems unlikely as axonal Ca_v2^{GFP} label is reduced in stj^{RNAi} . By contrast, $d\alpha_2\delta_1$ specifically reduces dendritic but not axonal Ca^{2+} entry, which suggests a more specific role of $d\alpha_2\delta_1$ for targeting VGCCs to the dendritic domain. Reduced Ca_v2 channel targeting to dendrites in $d\alpha_2\delta_1^{RNAi}$ is further supported by concomitant dendritic growth defects (Fig. 6). It has previously been demonstrated that Ca_v2 channels are required for local (Ryglewski et al., 2017) and for global dendritic growth regulation (Ryglewski et al., 2014; Vonhoff et al., 2013) in *Drosophila* DLM flight MNs. Similar to RNAi knock down of Ca_v2 channels (Ryglewski et al., 2014) in the DLM MN5 $d\alpha_2\delta_1^{RNAi}$ causes a significant decrease in total dendritic length (TDL, Fig. 6C) and in the number of branches (# branches, Fig. 6D) as revealed by intracellular dye fill and subsequent quantitative dendritic architecture analysis (Vonhoff and Duch, 2010). By contrast, mean dendritic branch length (MDL) and mean path length (MPL) are not affected (Figs. 6F-H). Therefore, $d\alpha_2\delta_1^{RNAi}$ does not seem to affect dendritic territory borders or dendritic branch elongation, but causes a significant reduction in new dendritic branch formation or maintenance which results in reduced total length.

Discussion

In this study we find that $d\alpha_2\delta_1$ and $d\alpha_2\delta_3$ (*stj*) are broadly expressed in the *Drosophila* nervous system. Despite differential expression patterns through the ventral nerve cord, both are co-expressed in the same motoneurons where they localize to different sub-neuronal compartments

and mediate different functions. $\alpha_2\delta_3$ (*stj*) is required for normal motoneuron presynaptic function and full somatodendritic and axonal Ca_v1 and Ca_v2 current amplitudes. By contrast, $\alpha_2\delta_1$ is not required for pre-synaptic function or full calcium current amplitudes, but by contrast, for the correct relative Ca_v2 channel allocation to the dendritic versus the axonal domain. Therefore, our *in vivo* analysis indicates that different $\alpha_2\delta$ subunits are required in the same neurons to regulate distinctly different functions of voltage gated Ca^{2+} channels. This contrasts findings in heterologous expression systems, where any HVA channel requires co-expression of any $\alpha_2\delta$ subunit for proper current amplitudes (Dolphin, 2012), but it is in agreement with different brain diseases resulting from specific mutations of single $\alpha_2\delta$ subunits. This underscores the importance for *in vivo* studies to unravel the combinatorial code by which different $\alpha_2\delta/\alpha_1$ interactions mediate functional Ca^{2+} channel diversity in different types of neurons and different sub-neuronal compartments.

*$\alpha_2\delta_1$ and $\alpha_2\delta_3$ (*stj*) mediate distinctly different functions in the CNS and in the same neurons*

Mutations in single mammalian $\alpha_2\delta$ genes are known causes to multiple brain diseases (Calandre et al., 2016; Davies et al., 2007; Klugbauer et al., 2003), thus indicating that loss of function of one $\alpha_2\delta$ subunit cannot be compensated for by others. Similarly, $\alpha_2\delta_3$ null mutant animals are embryonic lethal (Dickman et al., 2008; Ly et al., 2008; Kurshan et al., 2009). In addition, we find that $\alpha_2\delta_3^{\text{RNAi}}$ targeted specifically to flight motoneurons causes inability to fly, $\alpha_2\delta_1^{\text{RNAi}}$ significantly reduces *Drosophila* climbing speed, and pan-neural RNAi knock down of either or $\alpha_2\delta_3$ or $\alpha_2\delta_1$ does not cause compensatory up-regulation of the expression levels of the other one. Together these findings indicate differential and non-redundant functions of $\alpha_2\delta_1$ and $\alpha_2\delta_3$ (*stj*). On the contrary, in heterologous expression systems co-expression of multiple different $\alpha_2\delta$ subunits each can support the same HVA current (Dolphin, 2012), indicating that in principle, different $\alpha_1/\alpha_2\delta$ combinations can mediate similar functions, at least with regard to channel biophysical properties and surfacing. However, *in vivo*, redundant functions of multiple different $\alpha_1/\alpha_2\delta$ combinations seems unlikely, because differential spatial expression of different $\alpha_2\delta$ subunits has been reported for vertebrate brain (Scott and Kammermeier 2017; Nieto-Rostro et al., 2014; Cole et al., 2005). Similarly, we find differential expression patterns of $\alpha_2\delta_1$ and *stj* in the *Drosophila* ventral nerve cord. $\alpha_2\delta_1$ is strongly expressed in all central neuropils and in many neuronal somata, whereas $\alpha_2\delta_3$ was not detected in central neuropils but in many neuronal somata and in motoneuron axon terminals at the neuromuscular junction (Dickman et al., 2008; Ly et al., 2008; Kurshan et al., 2009). Notably, in *Drosophila* motoneurons both $\alpha_2\delta_1$ and $\alpha_2\delta_3$ are co-expressed, but localize to different sub-neuronal compartments. $\alpha_2\delta_3$ but not $\alpha_2\delta_1$ localizes at axon terminals and is required for pre-synaptic function (Wang et al., 2016; this study) and embryonic synapse development (Kurshan et al., 2009). Moreover, we find that $\alpha_2\delta_3$ and $\alpha_2\delta_1$ affect different aspects of motoneuron calcium channel function (see below).

*$\alpha_2\delta_3$ (*stj*) is required for normal Ca_v1 and Ca_v2 currents in all sub-neuronal compartments*

$\alpha_2\delta_3$ has previously been reported essential for *Drosophila* neuromuscular synapse development and function. During embryonic development loss of $\alpha_2\delta_3$ (*stj*) function impairs early steps of synapse formation before calcium channels arrive at the presynaptic terminal, as well as the subsequent recruitment of Ca_v2 -like channels to the active zone (Kurshan et al., 2009). Moreover, at mature larval neuromuscular junctions, $\alpha_2\delta_3$ is required for rapid induction and continuous expression of pre-synaptic homeostatic potentiation (Wang et al., 2016). Our data demonstrate that $\alpha_2\delta_3$ is not only required for Ca_v2 channel function at the pre-synaptic terminal, but also for normal flight motoneuron somatodendritic and axonal calcium currents, both of which are mediated by the *Drosophila* Ca_v2 channel homolog cacophony (Ryglewski et al., 2012; 2014). In addition, $\alpha_2\delta_3$ is required for normal larval motoneuron somatodendritic Ca_v1 current amplitudes encoded by the L-

type channel homolog *Dmca1D* (Worrell and Levine, 2008; Kadas et al., 2017; Schützler et al., 2019). Therefore, $\alpha_2\delta_3$ (stj) is required for normal calcium current amplitudes in *Drosophila* motoneurons independent of sub-neuronal compartment or Ca_v1 or Ca_v2 channel, thus indicating a general function in Ca_v1 and Ca_v2 channel surfacing. An important role for channel surfacing has also been reported for vertebrate $\alpha_2\delta_1$ (D'Arco et al., 2015; Cassidy et al., 2014).

$\alpha_2\delta_1$ specifically sets dendritic calcium channel abundance

Although somatodendritic calcium current amplitude is reduced by $d\alpha_2\delta_3^{RNAi}$ but unaffected by $d\alpha_2\delta_1^{RNAi}$, our data indicate that $\alpha_2\delta_1$ affects the relative allocation of calcium channels to the axonal versus the dendritic domain. Please note that voltage clamp recordings from the soma reflect the sum of proximal and more distal currents, but cannot precisely detect relative shifts in channel localization. Functional imaging reveals that both, targeted RNAi knock down of $d\alpha_2\delta_1$ and $d\alpha_2\delta_3$ significantly reduce the amplitude of dendritic calcium signals as evoked by action potential firing. By contrast, axonal calcium signals as evoked by the same firing patterns are nearly eliminated by $d\alpha_2\delta_3^{RNAi}$ but significantly increased by $d\alpha_2\delta_1^{RNAi}$. This again demonstrates different functions of $d\alpha_2\delta_1$ and $d\alpha_2\delta_3$ in the same neurons. Reduced dendritic and axonal calcium signals upon $d\alpha_2\delta_3^{RNAi}$ down are in line with a general function of stj in channel surfacing (see above). By contrast, increased axonal but decreased dendritic calcium signals following $d\alpha_2\delta_1^{RNAi}$ are in accord with a function of $\alpha_2\delta_1$ in channel sorting and/or targeting. One possibility is that $\alpha_2\delta_1$ serves linkage to specific motor proteins for transport to the dendritic domain. To us, the most parsimonious explanation for increased axonal calcium current amplitudes is that at a given rate of Ca_v2 channel production, reduced transport to dendrites in $d\alpha_2\delta_1^{RNAi}$ leaves increased channel numbers for the axon. By contrast, in mouse sensory neurons, knock-out of $\alpha_2\delta_1$ decreases axonal calcium channels (Margas et al., 2016). Please note that $\alpha_2\delta_1$ does not necessarily correspond to vertebrate $\alpha_2\delta_1$. Although *Drosophila* $\alpha_2\delta_1$ and $\alpha_2\delta_3$ contain the essential functional domains of vertebrate $\alpha_2\delta$ subunits, like the MIDAS motif, the von Willebrandt factor A (VWA), and the cache domains, sequence homology is not high enough to unambiguously match each vertebrate $\alpha_2\delta$ subunit with a specific *Drosophila* one. Based on functional analysis so far available one might speculate that vertebrate $\alpha_2\delta_1$ and *Drosophila* $\alpha_2\delta_3$ are functional pendants, because both are required for Ca_v2 channel targeting to axon terminals (Kurshan et al., 2009; Hoppa et al., 2012), both increase calcium channel abundance in the axonal membrane (this study; Margas et al., 2016), both increase $\text{Cav}2$ current amplitude (this study; D'Arco et al., 2015), and both play roles in the development of excitatory synapses independent of calcium channel function (Kurshan et al., 2009; Eroglu et al., 2009; Risher et al., 2018).

References

- Bainbridge SP, Bownes M (1981) Staging the metamorphosis of *Drosophila melanogaster*. *J Embryol Exp Morphol* 66:57-80.
- Barclay J, Balaguero N, Mione M, Ackerman SL, Letts VA, Brodbeck J, Canti C, Meir A, Page KM, Kusumi K, Perez-Reyes E, Lander ES, Frankel WN, Gardiner RM, Dolphin AC, Rees M (2001) Ducky mouse phenotype of epilepsy and ataxia is associated with mutations in the *Cacna2d2* gene and decreased calcium channel current in cerebellar Purkinje cells. *J Neurosci* 21(16):6095–6104.
- Bauer CS, Nieto-Rostro M, Rahman W, Tran-Van-Minh A, Ferron L, Douglas L, Kadurin I, Sri Ranjan Y, Fernandez-Alacid L, Millar NS, Dickenson AH, Lujan R, Dolphin AC (2009) The increased trafficking of the calcium channel subunit $\alpha_2\delta_1$ to presynaptic terminals in neuropathic pain is inhibited by the $\alpha_2\delta_1$ ligand pregabalin. *J Neurosci* 29(13):4076-4088.

Brockhaus J, Schreitmüller M, Repetto D, Klatt O, Reissner C, Elmslie K, Heine M, Missler M (2018) α -Neurexins Together with $\alpha 2\delta$ -1 Auxiliary Subunits Regulate Ca^{2+} Influx through Cav2.1 Channels. *J Neurosci.* 38(38):8277-8294.

Brodbeck J, Davies A, Courtney JM, Meir A, Balaguero N, Canti C, Moss FJ, Page KM, Pratt WS, Hunt SP, Barclay J, Rees M, Dolphin AC (2002), The ducky mutation in *Cacna2d2* results in altered Purkinje cell morphology and is associated with the expression of a truncated alpha 2 delta-2 protein with abnormal function. *J Biol Chem* 277(10):7684-7693.

Buraei Z, Yang J (2010), The β subunit of voltage-gated Ca^{2+} channels. *Physiol Rev.* 90(4):1461-1506. Review.

Cantí C, Nieto-Rostro M, Foucault I, Heblich F, Wratten J, Richards MW, Hendrich J, Douglas L, Page KM, Davies A, Dolphin AC (2005) The metal-ion-dependent adhesion site in the Von Willebrand factor-A domain of alpha2delta subunits is key to trafficking voltage-gated Ca^{2+} channels. *Proc. Natl. Acad. Sci. U.S.A.* 102(32):11230–11235.

Calandre EP, Rico-Villademoros F, Slim M (2016) Alpha2delta ligands, gabapentin, pregabalin and mirogabalin: a review of their clinical pharmacology and therapeutic use. *Expert Rev Neurother.* 16(11):1263-1277. Review. Erratum in *Expert Rev Neurother.* 16(11):iii (2016).

Cassidy JS, Ferron L, Kadurin I, Pratt WS, Dolphin AC (2014) Functional exofacially tagged N-type calcium channels elucidate the interaction with auxiliary $\alpha 2\delta$ -1 subunits. *Proc Natl Acad Sci U.S.A.* 111(24):8979-8984.

Catterall WA (2011) Voltage-gated calcium channels. *Cold Spring Harb Perspect Biol.* 3(8):a003947. doi: 10.1101/cshperspect.a003947. Review.

Celli R, Santolini I, Guiducci M, van Luijtelaar G, Parisi P, Striano P, Gradini R, Battaglia G, Ngomba RT, Nicoletti F (2017) The $\alpha 2\delta$ Subunit and Absence Epilepsy: Beyond Calcium Channels? *Curr Neuropharmacol.* 15(6):918-925. Review.

Chen Y, Chen SR, Chen H, Zhang J, Pan HL (2019) Increased $\alpha 2\delta$ -1-NMDA receptor coupling potentiates glutamatergic input to spinal dorsal horn neurons in chemotherapy-induced neuropathic pain. *J Neurochem.* 148(2):252-274.

Chen TW, Wardill TJ, Sun Y, Pulver SR, Renninger SL, Baohan A, Schreiter ER, Kerr RA, Orger MB, Jayaraman V, Looger LL, Svoboda K, Kim DS (2013) Ultrasensitive fluorescent proteins for imaging neuronal activity. *Nature.* 499(7458):295-300.

Cole RL, Lechner SM, Williams ME, Prodanovich P, Bleicher L, Varney MA, Gu G (2005) Differential Distribution of Voltage-Gated Calcium Channel Alpha-2 Delta ($\alpha 2\delta$) Subunit mRNA-Containing Cells in the Rat Central Nervous System and the Dorsal Root Ganglia. *J Comp. Neurol.* 491:246-269.

D'Arco M, Margas W, Cassidy JS, Dolphin AC (2015) The upregulation of $\alpha 2\delta$ -1 subunit modulates activity-dependent Ca^{2+} signals in sensory neurons. *J Neurosci.* 35(15):5891-5903.

Davies A, Douglas L, Hendrich J, Wratten J, Tran-Van-Minh A, Foucault I, Koch D, Pratt WS, Saibil H, Dolphin AC (2006) The calcium channel $\alpha 2\delta$ -2 subunit partitions with Cav2.1 in lipid rafts in cerebellum: implications for localization and function, *J Neurosci.* 26:8748–8757.

Davies A, Hendrich J, Van Minh AT, Wratten J, Douglas L, Dolphin AC (2007) Functional biology of the alpha(2)delta subunits of voltage-gated calcium channels. *Trends Pharmacol Sci.* 28(5):220-228. Review.

Davies A, Kadurin I, Alvarez-Laviada A, Douglas L, Nieto-Rostro M, Bauer CS, Pratt WS, Dolphin AC (2010) The $\alpha 2\delta$ subunits of voltage-gated calcium channels form GPI anchored proteins, a posttranslational modification essential for function. *Proc. Natl. Acad. Sci. U.S.A.* 107(4):1654–1659.

Dickman DK, Kurshan PT, Schwarz TL (2008) Mutations in a *Drosophila* alpha2delta voltage-gated calcium channel subunit reveal a crucial synaptic function. *J Neurosci.* 28(1):31-38.

Dietzl G, Chen D, Schnorrer F, Su KC, Barinova Y, Fellner M, Gasser B, Kinsey K, Ooppel S, Scheiblaue S, Couto A, Marra V, Keleman K, Dickson BJ (2007) A genome-wide transgenic RNAi library for conditional gene inactivation in *Drosophila*. *Nature.* 448(7150):151-156.

Dolphin AC (2012) Calcium channel $\alpha 2\delta$ subunits in epilepsy and as targets for antiepileptic drugs” in Jasper’s Basic Mechanisms of the Epilepsies [Internet]. J. L. Noebels, M. Avoli, M. A. Rogawski, R. W. Olsen, A. V. Delgado-Escueta, Eds. 4th edition. (Bethesda (MD): National Center for Biotechnology Information (US), 2012).

Dolphin AC (2013) The $\alpha 2\delta$ subunits of voltage-gated calcium channels. *Biochim Biophys Acta.* 1828(7):1541-1549.

Eroglu C, Allen NJ, Susman MW, O'Rourke NA, Park CY, Ozkan E, Chakraborty C, Mulinyawe SB, Annis DS, Huberman AD, Green EM, Lawler J, Dolmetsch R, Garcia KC, Smith SJ, Luo ZD, Rosenthal A, Mosher DF, Barres BA (2009) Gabapentin receptor alpha2delta-1 is a neuronal thrombospondin receptor responsible for excitatory CNS synaptogenesis. *Cell* 139(2):380-392.

Evers JF, Schmitt S, Sibila M, Duch C (2005) Progress in functional neuroanatomy: precise automatic geometric reconstruction of neuronal morphology from confocal image stacks. *J Neurophysiol* 93(4):2331-2342.

Faria LC, Gu F, Parada I, Barres B, Luo ZD, Prince DA (2017) Epileptiform activity and behavioral arrests in mice overexpressing the calcium channel subunit $\alpha 2\delta$ -1. *Neurobiol Dis.* 102:70-80.

Felix R, Gurnett CA, De Waard M, Campbell KP (1997) Dissection of functional domains of the voltage-dependent Ca^{2+} channel alpha2delta subunit. *J Neurosci* 17(18):6884–6891.

Fell B, Eckrich S, Blum K, Eckrich T, Hecker D, Obermair GJ, Münkner S, Flockerzi V, Schick B, Engel J (2016) $\alpha 2\delta 2$ Controls the Function and Trans-Synaptic Coupling of Cav1.3 Channels in Mouse Inner Hair Cells and Is Essential for Normal Hearing. *J Neurosci.*36(43):11024-11036.

Feng Y, Ueda A, Wu CF (2004) A modified minimal hemolymph-like solution, HL3.1, for physiological recordings at the neuromuscular junctions of normal and mutant *Drosophila* larvae. *J Neurogenet* 18(2):377-402.

Ferron L, Kadurin I, Dolphin AC (2018) Proteolytic maturation of $\alpha 2\delta$ controls the probability of synaptic vesicular release. *Elife* 7. pii: e37507 (2018). doi: 10.7554/eLife.37507.

Gratz SJ, Goel P, Bruckner JJ, Hernandez RX, Khateeb K, Macleod GT, Dickman D, O'Connor-Giles KM (2019) Endogenous Tagging Reveals Differential Regulation of Ca^{2+} Channels at Single Active Zones during Presynaptic Homeostatic Potentiation and Depression. *J Neurosci* 39(13):2416-2429.

Green EW, Fedele G, Giorgini F, Kyriacou CP (2014) A *Drosophila* RNAi collection is subject to dominant phenotypic effects. *Nat Methods* 11(3):222-223.

Hendrich J, Tran-Van-Minh A, Heblich F, Nieto-Rostro M, Watschinger K, Striessnig J, Wratten J, Davies A, Dolphin AC (2008) Pharmacological disruption of calcium channel trafficking by the $\alpha 2\delta$ ligand gabapentin, *Proc. Natl. Acad. Sci. U.S.A.* 105:3628–3633.

- Hobom M, Dai S, Marais E, Lacinova L, Hofmann F, Klugbauer N (2000) Neuronal distribution and functional characterization of the calcium channel $\alpha 2\delta$ -2 subunit. *Eur J Neurosci* 12(4):1217-1226.
- Hoppa MB, Lana B, Margas W, Dolphin AC, Ryan TA (2012) $\alpha 2\delta$ expression sets presynaptic calcium channel abundance and release probability. *Nature* 486(7401):122-125.
- Kadas D, Klein A, Krick N, Worrell JW, Ryglewski S, Duch C (2017) Dendritic and Axonal L-Type Calcium Channels Cooperate to Enhance Motoneuron Firing Output during *Drosophila* Larval Locomotion. *J Neurosci* 37(45):10971-10982.
- Kadurin I, Rothwell SW, Lana B, Nieto-Rostro M, Dolphin AC (2017) LRP1 influences trafficking of N-type calcium channels via interaction with the auxiliary $\alpha 2\delta$ -1 subunit. *Sci Rep* 7:43802 (2017). doi: 10.1038/srep43802.
- Kawasaki F, Zou B, Xu X, Ordway RW (2004) Active zone localization of presynaptic calcium channels encoded by the cacophony locus of *Drosophila*. *J Neurosci* 24(1):282-285.
- Kittel RJ, Wichmann C, Rasse TM, Fouquet W, Schmidt M, Schmid A, Wagh DA, Pawlu C, Kellner RR, Willig KI, Hell SW, Buchner E, Heckmann M, Sigrist SJ, Bruchpilot promotes active zone assembly, Ca^{2+} channel clustering, and vesicle release. *Science* 312(5776):1051-1054.
- Klugbauer N, Marais E, Hofmann F (2003) Calcium channel $\alpha 2\delta$ subunits: differential expression, function, and drug binding. *J Bioenerg Biomembr* 35(6):639-647. Review.
- Kurshan PT, Oztan A, Schwarz TL (2009) Presynaptic $\alpha 2\delta$ -3 is required for synaptic morphogenesis independent of its Ca^{2+} -channel functions. *Nat Neurosci* 12(11):1415-1423.
- Littleton JT, Ganetzky B (2000) Ion channels and synaptic organization: analysis of the *Drosophila* genome. *Neuron* 26(1):35-43.
- Ly CV, Yao CK, Verstreken P, Ohyama T, Bellen HJ (2008) straightjacket is required for the synaptic stabilization of cacophony, a voltage-gated calcium channel $\alpha 1$ subunit. *J Cell Biol* 181(1):157-70.
- Margas W, Ferron L, Nieto-Rostro M, Schwartz A, Dolphin AC (2016) Effect of knockout of $\alpha 2\delta$ -1 on action potentials in mouse sensory neurons. *Philos Trans R Soc Lond B Biol Sci.* 371(1700) (2016). pii: 20150430. doi: 10.1098/rstb.2015.0430.
- Nagarkar-Jaiswal S, Lee PT, Campbell ME, Chen K, Anguiano-Zarate S, Cantu Gutierrez M, Busby T, Lin WW, He Y, Schulze KL, Booth BW, Evans-Holm M, Venken KJ, Levis RW, Spradling AC, Hoskins RA, Bellen HJ (2015) A library of MiMICs allows tagging of genes and reversible, spatial and temporal knockdown of proteins in *Drosophila*. *eLife* 4: e05338 (2015). doi:10.7554/eLife.05338.
- Nieto-Rostro M, Ramgoolam K, Pratt WS, Kulik A, Dolphin AC (2018) Ablation of $\alpha 2\delta$ -1 inhibits cell-surface trafficking of endogenous N-type calcium channels in the pain pathway in vivo. *Proc Natl Acad Sci U.S.A.* 115(51):E12043-E12052.
- Nieto-Rostro M, Sandhu G, Bauer CS, Jiruska P, Jefferys JG, Dolphin AC (2014) Altered expression of the voltage-gated calcium channel subunit $\alpha 2\delta$ -1: a comparison between two experimental models of epilepsy and a sensory nerve ligation model of neuropathic pain. *Neuroscience* 283:124-137.
- Perkins LA, Holderbaum L, Tao R, Hu Y, Sopko R, McCall K, Yang-Zhou D, Flockhart I, Binari R, Shim HS, Miller A, Housden A, Foos M, Randkelv S, Kelley C, Namgyal P, Villalta C, Liu LP, Jiang X, Huan-Huan Q, Wang X, Fujiyama A, Toyoda A, Ayers K, Blum A, Czech B, Neumuller R, Yan D, Cavallaro A, Hibbard K, Hall D, Cooley L, Hannon GJ, Lehmann R, Parks A, Mohr SE, Ueda R, Kondo S, Ni JQ, Perrimon N

(2015) The Transgenic RNAi Project at Harvard Medical School: Resources and Validation. *Genetics* 201(3): 843-852.

Reuveny A, Shnayder M, Lorber D, Wang S, Volk T (2018) Ma2/d promotes myonuclear positioning and association with the sarcoplasmic reticulum. *Development* 28:145(17). doi: 10.1242/dev.159558.

Risher WC, Kim N, Koh S, Choi JE, Mitev P, Spence EF, Pilaz LJ, Wang D, Feng G, Silver DL, Soderling SH, Yin HH, Eroglu C (2018) Thrombospondin receptor $\alpha 2\delta$ -1 promotes synaptogenesis and spinogenesis via postsynaptic Rac1. *J Cell Biol* 217(10):3747-3765.

Ryglewski S, Duch C (2012b) Preparation of *Drosophila* central neurons for in situ patch clamping. *J Vis Exp*. 2012 Oct 15;(68). pii: 4264. doi: 10.3791/4264.S.

Ryglewski S, Kilo L, Duch C (2014) Sequential acquisition of cacophony calcium currents, sodium channels and voltage-dependent potassium currents affects spike shape and dendrite growth during postembryonic maturation of an identified *Drosophila* motoneuron. *Eur J Neurosci* 39(10):1572-1585.

Ryglewski S, Lance K, Levine RB, Duch C (2012) Ca(v)2 channels mediate low and high voltage-activated calcium currents in *Drosophila* motoneurons. *J Physiol* 590(4):809-258.

Ryglewski S, Vonhoff F, Scheckel K, Duch C (2017) Intra-neuronal Competition for Synaptic Partners Conserves the Amount of Dendritic Building Material. *Neuron* 93(3):632-645.

Savalli N, Pantazis A, Sigg D, Weiss JN, Neely A, Olcese R (2016) The $\alpha 2\delta$ -1 subunit remodels CaV1.2 voltage sensors and allows Ca²⁺ influx at physiological membrane potentials. *J Gen Physiol* 148(2):147-159.

Schmitt S, Evers JF, Duch C, Scholz M, Obermayer K (2004) New methods for the computer-assisted 3-D reconstruction of neurons from confocal image stacks. *Neuroimage* 23(4): 1283-1298.

Schützler N, Girwert C, Hügli I, Mohana G, Roignant JY, Ryglewski S, Duch C (2019) Tyramine action on motoneuron excitability and adaptable tyramine/octopamine ratios adjust *Drosophila* locomotion to nutritional state. *Proc Natl Acad Sci U.S.A.* 116(9):3805-3810.

Scott MB, Kammermeier PJ (2017) CaV2 channel subtype expression in rat sympathetic neurons is selectively regulated by $\alpha 2\delta$ subunits. *Channels (Austin)*. 11(6):555-573.

Tong XJ, López-Soto EJ, Li L, Liu H, Nedelcu D, Lipscombe D, Hu Z, Kaplan JM (2017) Retrograde Synaptic Inhibition Is Mediated by α -Neurexin Binding to the $\alpha 2\delta$ Subunits of N-Type Calcium Channels. *Neuron* 95(2):326-340.

Venken KJ, Schulze KL, Haelterman NA, Pan H, He Y, Evans-Holm M, Carlson JW, Levis RW, Spradling AC, Hoskins RA, Bellen HJ (2011) MiMIC: a highly versatile transposon insertion resource for engineering *Drosophila melanogaster* genes. *Nat Methods* 8(9):737-743.

Vonhoff F, Duch C (2010) Tiling among stereotyped dendritic branches in an identified *Drosophila* motoneuron. *J Comp Neurol* 518(12):2169-2185.

Vonhoff F, Kuehn C, Blumenstock S, Sanyal S, Duch C (2013) Temporal coherency between receptor expression, neural activity and AP-1-dependent transcription regulates *Drosophila* motoneuron dendrite development. *Development* 140(3):606-616.

Wagh DA, Rasse TM, Asan E, Hofbauer A, Schwenkert I, Dürrbeck H, Buchner S, Dabauvalle MC, Schmidt M, Qin G, Wichmann C, Kittel R, Sigrist SJ, Buchner E (2006) Bruchpilot, a protein with

homology to ELKS/CAST, is required for structural integrity and function of synaptic active zones in *Drosophila*. *Neuron* 49(6):833-844. Erratum in: *Neuron* 51(2):275 (2006).

Wang T, Jones RT, Whippen JM, Davis GW (2016) $\alpha 2\delta$ -3 Is Required for Rapid Transsynaptic Homeostatic Signaling. *Cell Rep* 16(11):2875-2888.

Worrell JW, Levine RB (2008) Characterization of voltage-dependent Ca^{2+} currents in identified *Drosophila* motoneurons in situ. *J Neurophysiol* 100(2):868-878.

Figure legends

Figure 1: *stj* and $\alpha_2\delta_1$ are differentially expressed in the *Drosophila* CNS but co-localize in motoneurons (MNs).

(A-Aii) Projection view of 40 dorsal optical sections from a representative confocal image stack of the larval ventral nerve cord (VNC). (A) *stj*^{mCherry} (green) and (Ai) $\alpha_2\delta_1$ ^{GFP} (magenta) are both expressed in many somata in the ganglionic cortex of the larval VNC, including overlapping expression in crawling MNs. (Aii) Neuropil is labeled with the synaptic marker *brp* (cyan). No *stj*^{mCherry} (A, green) but abundant $\alpha_2\delta_1$ ^{GFP} (Ai, magenta) was found in the neuropil. (Aiii, Aiv, Merge) For better visualization of expression in MN somata five sections were selectively enlarged at the regions marked by white rectangles in (A) and (Ai). Expression of both *stj*^{mCherry} (Aiii) and $\alpha_2\delta_1$ ^{GFP} (Aiv) in larval crawling MNs (white arrows). The (Merge) shows an overlay of (Aiii) and (Aiv) revealing co-label in MNs. (B-Bii) Same representative preparations as in (A-Aii), but deeper in the VNC and at higher magnification to visualize neuropil regions. (B) The neuropil is devoid of *stj*^{mCherry} (green), which is localized only to somata in the ganglionic cortex. (Bi) $\alpha_2\delta_1$ ^{GFP} (magenta) is abundantly expressed in VNC synaptic neuropil that is counterstained with *brp* (Bii, cyan). (C) *stj*-HA is expressed under the control of the *stj* promoter (*stj*-GAL4>UAS-*stj*-HA) in the larval VNC. Neuropil label is not detectable, but *stj*-HA is found in many somata in the larval VNC including MNs (asterisks). (D-E) Adult VNC. (D) *stj*^{mCherry} (green) and $\alpha_2\delta_1$ ^{GFP} (Di, magenta) are expressed in somata in the ganglionic cortex. (Di, Dii) $\alpha_2\delta_1$ ^{GFP} is abundantly expressed in neuropil regions (Di, magenta) which are co-labeled with the synaptic marker *brp* (Dii, cyan). (E) Expression of *stj* (green) in adult wing depressor MNs (white arrowheads). (Ei) High expression levels of $\alpha_2\delta_1$ (magenta) in neuropil (Eii, *brp*, cyan) results in low contrast for detection in adult wing MNs. Localization of DLM MN5 is indicated by dotted white circles and arrow heads (E, Ei). (F, Fi) Therefore, expression of $\alpha_2\delta_1$ ^{GFP} in wing depressor MNs was also confirmed in pupal stage P14, shortly before adult eclosion (see dotted white line in (F) and in the enlargement in (Fi)). (G) *stj*-HA expressed under the control of *stj*-GAL4 is detectable in adult DLM MNs (arrows) and in other somata.

Figure 2: *stj* and $\alpha_2\delta_1$ do not compensate for each other on the protein level.

(A, Ai) Analysis of *stj* and $\alpha_2\delta_1$ RNAi knock down efficacy. (A) Western blotting shows effective knock down of *stj*^{mCherry} (left two lanes) and of $\alpha_2\delta_1$ ^{GFP} (right two lanes) following pan-neurally expressed *UAS-stj*^{RNAi} and *UAS- $\alpha_2\delta_1$* ^{RNAi} transgenes (*elav*^{c155}-GAL4>UAS-RNAi; *UAS-dcr2*). The respective control lanes show two bands, because a fraction of $\alpha_2\delta$ is cleaved into α_2 and δ . The upper $\alpha_2\delta$ band corresponds to un-cleaved $\alpha_2\delta$, the lower band to cleaved α_2 that carries the mCherry (*stj*) or GFP-tag ($\alpha_2\delta_1$), respectively. (Ai) Quantification reveals 64% knock down efficacy for *stj* (control and knock down, left two bars), and 98% knock down on the protein level for $\alpha_2\delta_1$ (right two bars). Numbers in bars indicate number of replicates. (B) *$\alpha_2\delta_1$* ^{RNAi} reduces climbing speed. In a negative geotaxis assay, pan-neural *$\alpha_2\delta_1$* ^{RNAi} results in a 40% median reduction in climbing speed from 2.3 to 1.4 cm/s as compared to control (N for control: 52, for *$\alpha_2\delta_1$* ^{RNAi}: 21; $p < 0.001$, Mann-Whitney U-test). Boxes represent median and 25 and 75% quartiles. Whiskers represent 10 and 90% quartiles. (C, D) *stj* and $\alpha_2\delta_1$ do not compensate for each other when either one is knocked down via pan-neural RNAi. *stj*^{RNAi} does not affect $\alpha_2\delta_1$ protein level (C, $p = 1$, Mann-Whitney U-test), and vice versa, *$\alpha_2\delta_1$* ^{RNAi} does not affect *stj* protein level as analyzed by Western Blot (D, $p = 0.78$, Mann-Whitney U-test). Data in (C) and (D) are presented as single data point with median.

Figure 3: *stj* but not $\alpha_2\delta_1$ is required for normal MN Ca_v1 -like and Ca_v2 -like current amplitudes in vivo.

(A, Ai) Analysis of larval EPSPs. **(A)** Effect of *stj*^{RNAi} and of $\alpha_2\delta_1$ ^{RNAi} targeted only to MNs (*vGlut*^{OK371-GAL4>UAS-RNAi; UAS-dcr2) on larval neuromuscular synaptic transmission was tested in sharp electrode muscle recordings of muscle 10. EPSPs were monitored following extracellular MN stimulation. *stj*^{RNAi} (middle trace) but not $\alpha_2\delta_1$ ^{RNAi} (right trace) caused a reduction in EPSP amplitude as compared to control (left trace). **(Ai)** Quantification revealed a ~50% and highly significant reduction in EPSP amplitude by *stj*^{RNAi} (light gray box) as compared to control (white box), but $\alpha_2\delta_1$ ^{RNAi} had no effect (dark gray box). control n=17, *stj*^{RNAi} n=11, $\alpha_2\delta_1$ ^{RNAi} n=14; **p=0.001, Kruskal Wallis ANOVA with Dunn's post hoc test). Boxes display median with 25 and 75% quartiles, whiskers represent 10 and 90% quartiles. **(B-I)** Whole cell Ca^{2+} current recorded from larval crawling **(B-C)**, adult **(D-G)**, and pupal DLM MNs **(H-I)** *in situ*. Currents were elicited from a holding potential of -90 mV in 10 mV command voltage steps of 200 ms duration to 0 mV (larva) or +20 mV (adult and pupae) using blockers for Na^+ and K^+ channels. For voltage protocols see insets in **(B)**, **(D)** and **(Hii)**. As compared to control **(B, C, n=13)** larval somatodendritic Ca_v1 -like current amplitude was reduced by 46% following *stj*^{RNAi} **(Bi, C, n=14; ***p=1.4*10⁻⁴**, one-way ANOVA with LSD post hoc test) but not by $\alpha_2\delta_1$ ^{RNAi} **(Bii, C, n=7)**. **(D-I)** Adult and pupal Ca^{2+} currents were recorded from DLM MN5. Knock down was driven specifically in DLM MNs by *23H06-GAL4>UAS-RNAi; UAS-dcr2*. **(D-G)** Adult Ca_v2 Ca^{2+} current. As compared to control **(D, n = 5)** adult HVA Ca_v2 current was reduced by ~60% following *stj*^{RNAi} **(Di, F, n=5, **p=0.006**, one-way ANOVA with LSD post hoc test), but unaffected by $\alpha_2\delta_1$ ^{RNAi} **(Dii, G, n=5)**. **(E)** Adult low voltage activated (LVA) Ca_v2 current (control, left trace) was reduced by 36% following *stj*^{RNAi} **(E, middle trace, G, *p=0.025**, one-way ANOVA with LSD post hoc test) but unaffected by $\alpha_2\delta_1$ ^{RNAi} **(Dii, G)**. **(H-I)** Pupal stage P8 (P50%) HVA Ca_v2 current. Pupal Ca_v2 current was reduced by 53% on average following *stj*^{RNAi} **(H, Hi, I, white and light gray bars, control n=11; *stj*^{RNAi} n=13, ***p=3.6*10⁻⁵**, one-way ANOVA with LSD post hoc test) but unaffected by $\alpha_2\delta_1$ ^{RNAi} **(Hii, I, dark gray bar, n=7)**. Double *stj*^{RNAi}/ $\alpha_2\delta_1$ ^{RNAi} did not reveal additional effects and reduced Ca_v2 current amplitude by ~43% as compared to control **(Hiii, I, black bar, n=6; **p = 0.005**, one-way ANOVA with LSD post hoc test). Data in **(C)**, **(F)**, **(G)**, and **(I)** are represented as means \pm SD.}

Figure 4: *stj*^{RNAi} and $\alpha_2\delta_1$ ^{RNAi} affect normal function of axonal Ca_v2 channels differently.

(A) As compared to control (top panel) *stj*^{RNAi} (middle panel) decreases endogenous Ca_v2 ^{GFP} label in DLM MN axons (encircled by dotted white line), whereas $\alpha_2\delta_1$ ^{RNAi} (bottom panel) increases label. **(B)** Quantification of mean gray of Ca_v2 ^{GFP} puncta in confocal sections revealed a ~20% and significant decrease in *stj*^{RNAi} (light gray bar, **p=0.006, n=9) but a ~20% and significant increase in $\alpha_2\delta_1$ ^{RNAi} (dark gray bar, **p=0.001, n=10) as compared to control (white bar, N=9). Error bars represent SD; statistical significance was determined with one-way ANOVA with LSD post-hoc test. **(C)** Pupal DLM MN action potentials (APs) were recorded in 1.8 and 5 mM Ca^{2+} saline and elicited by square pulse current injections. APs showed a Ca^{2+} shoulder (C, top, left trace, see arrow) that was abolished by the VGCC blocker Cd^{2+} (500 μ M; C, top, gray trace) and broadened in high Ca^{2+} (C, top, left trace). APs were smaller and narrower in *stj*^{RNAi} (C, middle, left two traces) as compared to control (C, top, left two traces) and were neither reduced or narrowed (D) nor broadened in high 5 mM Ca^{2+} saline (C, middle row, right trace). Following $\alpha_2\delta_1$ ^{RNAi} APs often showed a double peak (C, bottom, left trace) that was abolished in Cd^{2+} (C, bottom, gray trace), but APs were broadened in high Ca^{2+} saline (C, bottom, left trace). AP half width was reduced significantly more in control (p = 0.012) and following $\alpha_2\delta_1$ ^{RNAi} (p = 0.013) as compared to *stj*^{RNAi} (D, single data points and medians are presented). Statistical significance was determined by Kruskal-Wallis ANOVA with Dunn's post-hoc test).

Figure 5: Dendritic localization of VGCCs depends on $d\alpha_2\delta_1$.

(A) Changes in intracellular $[Ca^{2+}]$ ($\Delta F/F$) upon induced firing in different compartments of pupal DLM MNs. Regions of interest in dendrites and in the axon (inset in A, upper right corner) are indicated by arrows and white circles. (B, Bi) Change in fluorescence in dendrites is significantly reduced following both stj^{RNAi} (light gray circles; ** $p=0.003$, $n=11$) and $d\alpha_2\delta_1^{RNAi}$ (dark gray circles; *** $p<0.001$, $n=26$) as compared to control (B, white circles, $n=16$), whereas no statistical difference is found between stj^{RNAi} and $d\alpha_2\delta_1^{RNAi}$ (ns; B). By contrast, axonal Ca^{2+} signals are significantly reduced following stj^{RNAi} (light gray circles; *** $p<0.001$, $n=15$) but significantly increased following $d\alpha_2\delta_1^{RNAi}$ (** $p=0.001$, $N=11$) as compared to control (Bi, $N=19$). Change in fluorescence is significantly reduced following stj^{RNAi} as compared to $d\alpha_2\delta_1^{RNAi}$ (** $p<0.001$; Bi). Data in (B and Bi) are presented as single data points and median. Statistical significance was tested by Kruskal-Wallis ANOVA with Dunn's post-hoc test. (C-Di) Change in fluorescence ($\Delta F/F$) upon evoked AP firing in different neuronal compartments in control and following stj^{RNAi} and $d\alpha_2\delta_1^{RNAi}$. (C) APs were elicited by somatic ramp current injection of 400 ms duration and 1 nA amplitude (stimulation protocol see inset in C). (D) Dendritic Ca^{2+} signals are reduced approx. by half following both stj^{RNAi} (light gray trace) and $d\alpha_2\delta_1^{RNAi}$ (dark gray trace) as compared to control (black trace). (Di) Axonal Ca^{2+} signals are reduced following stj^{RNAi} (light gray trace) but increased following $d\alpha_2\delta_1^{RNAi}$ (light gray trace) as compared to control (black trace).

Figure 6: $d\alpha_2\delta_1$ affects dendrite development. (A, B) Reconstructions of adult MN5 dendrite in control (A, $n=3$) and following $d\alpha_2\delta_1^{RNAi}$ (B, $n=6$). (C-F) Morphometric parameters were analyzed. Following $d\alpha_2\delta_1^{RNAi}$ total dendritic length (C, TDL, $6580 \pm 408 \mu m$ vs. $5043 \pm 824 \mu m$; ** $p = 0.007$, Student's T-test) as well as the number of dendritic branches (D, # branches, 4421 ± 382 vs. 3122 ± 700 ; ** $p=0.009$, Student's T-test) are reduced. Other parameters like the mean dendrite length (E, MDL, 1.48 ± 0.09 vs. $1.67 \pm 0.11 \mu m$; $p=0.055$) and the mean path length (F, MPL, 9.05 ± 0.61 vs. $9.41 \pm 0.74 \mu m$; $p=0.468$) are not affected.

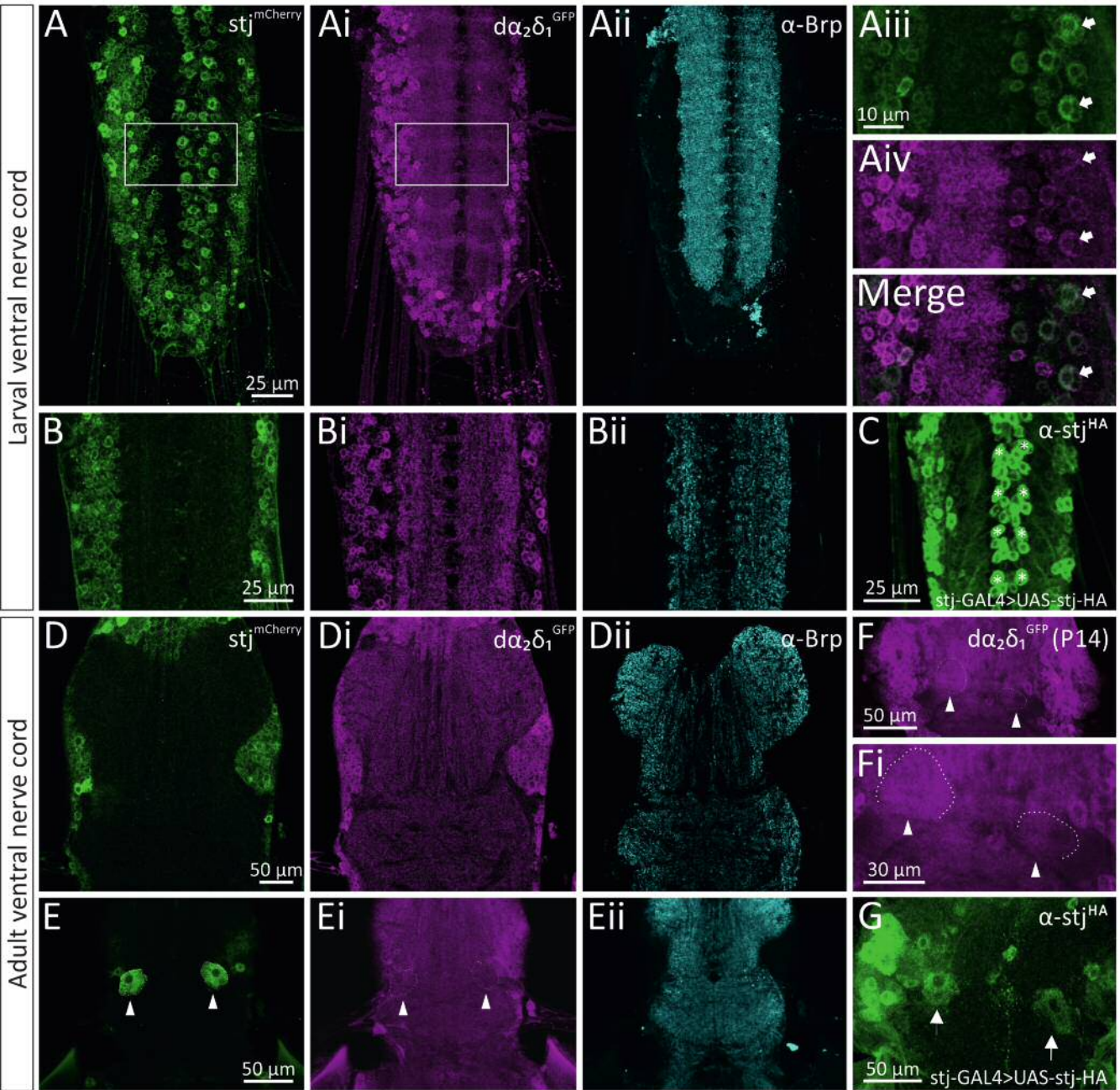


Figure 1, Heinrich, Ryglewski 2019

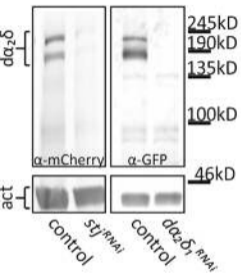
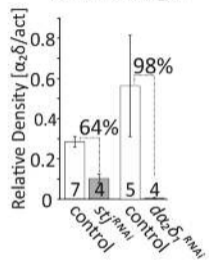
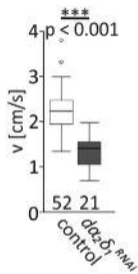
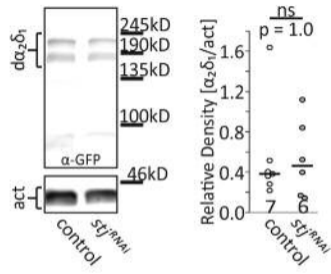
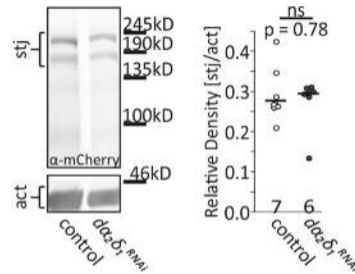
A RNAi validation**Ai** RNAi knock down strength**B** Climbing speed**C** $d\alpha_2\delta_1$ is not up-regulated in *stj*^{RNAi}**D** *stj* is not up-regulated in *dα2δ1*^{RNAi}

Figure 2, Heinrich, Ryglewski 2019

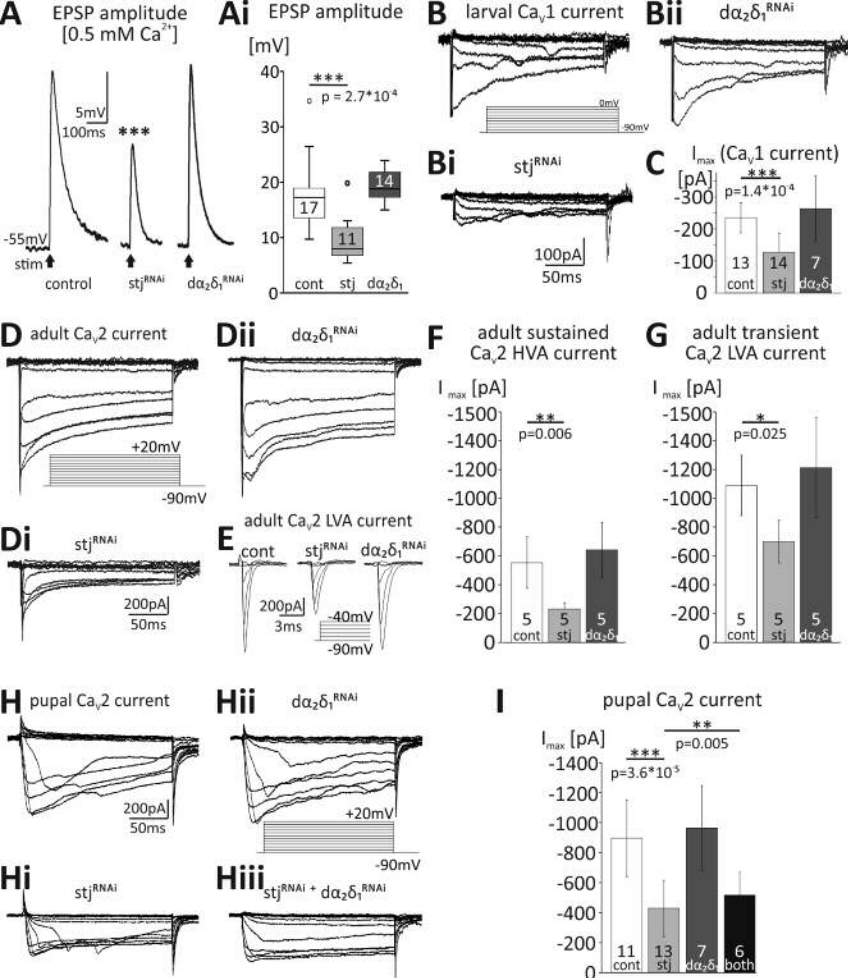


Figure 3, Heinrich, Ryglewski 2019

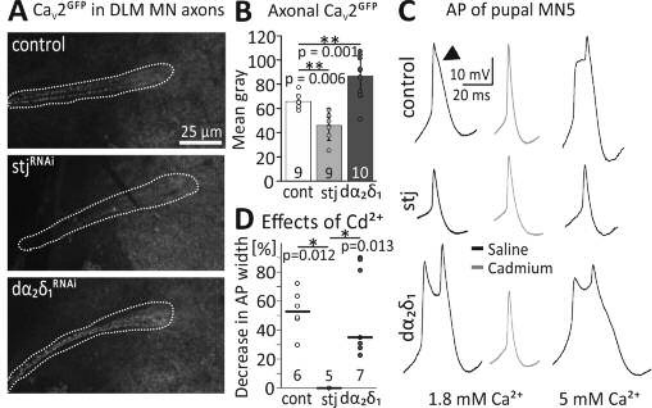


Figure 4, Heinrich, Ryglewski 2019

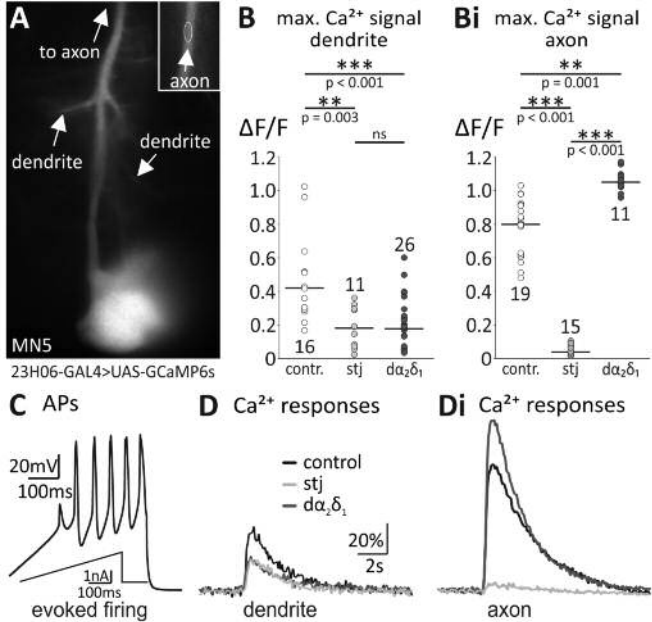


Figure 5, Heinrich, Ryglewski 2019

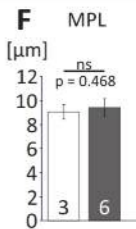
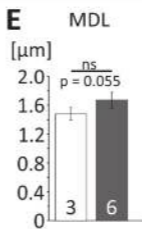
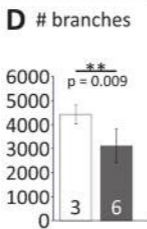
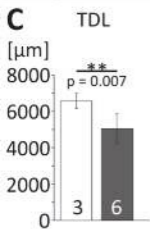
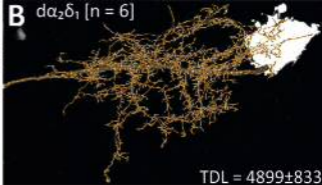
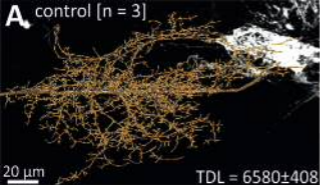


Figure 6, Heinrich, Ryglewski 2019